

# NOMAD spectrometer on the ExoMars trace gas orbiter mission: part 1—design, manufacturing and testing of the infrared channels

**EDDY NEEFS,<sup>1,\*</sup> ANN CARINE VANDAELE,<sup>1</sup> RACHEL DRUMMOND,<sup>1</sup> IAN R. THOMAS,<sup>1</sup> SOPHIE BERKENBOSCH,<sup>1</sup> ROLAND CLAIRQUIN,<sup>1</sup> SOFIE DELANOYE,<sup>1</sup> BOJAN RISTIC,<sup>1</sup> JEROEN MAES,<sup>1</sup> SABRINA BONNEWIJN,<sup>1</sup> GERRY PIECK,<sup>1</sup> EDDY EQUETER,<sup>1</sup> CÉDRIC DEPIESSE,<sup>1</sup> FRANK DAERDEN,<sup>1</sup> EMIEL VAN RANSBEECK,<sup>2</sup> DENNIS NEVEJANS,<sup>3</sup> JULIO RODRIGUEZ-GÓMEZ,<sup>4</sup> JOSÉ-JUAN LÓPEZ-MORENO,<sup>4</sup> ROSARIO SANZ,<sup>4</sup> RAFAEL MORALES,<sup>4</sup> GIAN PAOLO CANDINI,<sup>4</sup> M. CARMEN PASTOR-MORALES,<sup>4</sup> BEATRIZ APARICIO DEL MORAL,<sup>4</sup> JOSÉ-MARÍA JERÓNIMO-ZAFRA,<sup>4</sup> JUAN MANUEL GÓMEZ-LÓPEZ,<sup>4</sup> GUSTAVO ALONSO-RODRIGO,<sup>5</sup> ISABEL PÉREZ-GRANDE,<sup>5</sup> JAVIER CUBAS,<sup>5</sup> ALEJANDRO M. GOMEZ-SANJUAN,<sup>5</sup> FERMÍN NAVARRO-MEDINA,<sup>5</sup> TANGUY THIBERT,<sup>6</sup> MANISH R. PATEL,<sup>7,8</sup> GIANCARLO BELLUCCI,<sup>9</sup> LIEVE DE VOS,<sup>10</sup> STEFAN LESSCHAEVE,<sup>10</sup> NICO VAN VOOREN,<sup>10</sup> WOUTER MOELANS,<sup>10</sup> LUDOVIC ABALLEA,<sup>10</sup> STIJN GLORIEUX,<sup>10</sup> ANN BAEKE,<sup>10</sup> DAVE KENDALL,<sup>10</sup> JURGEN DE NEEF,<sup>10</sup> ALEXANDER SOENEN,<sup>10</sup> PIERRE-YVES PUECH,<sup>10</sup> JON WARD,<sup>11</sup> JEAN-FRANÇOIS JAMOYE,<sup>12</sup> DAVID DIEZ,<sup>13</sup> ANA VICARIO-ARROYO,<sup>13</sup> AND MICHEL JANKOWSKI<sup>14</sup>**

<sup>1</sup>Belgian Institute for Space Aeronomy, BIRA-IASB, Ringlaan 3, 1180 Brussels, Belgium

<sup>2</sup>VREC, Dries 15, 1745 Mazonzele, Belgium

<sup>3</sup>(formerly) CONSERD, Krekelstraat 27, 9052 Gent, Belgium

<sup>4</sup>Instituto de Astrofísica de Andalucía, IAA-CSIC, Glorieta de la Astronomía, 18008 Granada, Spain

<sup>5</sup>Universidad Politécnica de Madrid, IDR/UPM, Plaza Cardenal Cisneros 3, 28040 Madrid, Spain

<sup>6</sup>Centre Spatial de Liège, CSL, Liège Science Park, Avenue du Pré-Aily, 4031 Angleur, Belgium

<sup>7</sup>Department of Physical Sciences, The Open University, Milton Keynes, MK7 6AA, UK

<sup>8</sup>SSTD, STFC Rutherford Appleton Laboratory, Chilton, Oxfordshire OX11 0QX, UK

<sup>9</sup>Istituto di Astrofísica e Planetología Spaziali, IAPS-INAF, Via del Fosso del Cavaliere 100, 00133 Rome, Italy

<sup>10</sup>OIP, Westerring 21, 9700 Oudenaarde, Belgium

<sup>11</sup>Gooch and Housego, Dowlish Ford, Ilminster, TA19 0PF, UK

<sup>12</sup>AMOS, Rue des Chasseurs Ardennais 2, 4031 Angleur, Belgium

<sup>13</sup>ERZIA, Castelar 3, 39004 Santander, Spain

<sup>14</sup>Thales Alenia Space Belgium, Rue Chapelle Beaussart 101, 6032 Mont-sur-Marchienne, Belgium

\*Corresponding author: eddy.neefs@aeronomie.be

Received 4 June 2015; revised 12 August 2015; accepted 27 August 2015; posted 31 August 2015 (Doc. ID 242418); published 30 September 2015

NOMAD is a spectrometer suite on board ESA's ExoMars trace gas orbiter due for launch in January 2016. NOMAD consists of two infrared channels and one ultraviolet and visible channel allowing the instrument to perform observations quasi-constantly, by taking nadir measurements at dayside and nightside, and during solar occultations. In this paper, the design, manufacturing, and testing of the two infrared channels are described. We focus upon the optical working principle in these channels, where an echelle grating, used as a diffractive element, is combined with an acousto-optical tunable filter, used as a diffraction order sorter. © 2015 Optical Society of America

**OCIS codes:** (120.6085) Space instrumentation; (120.6200) Spectrometers and spectroscopic instrumentation; (120.0280) Remote sensing and sensors; (300.6340) Spectroscopy, infrared.

<http://dx.doi.org/10.1364/AO.54.008494>

## 1. INTRODUCTION

The Nadir and Occultation for MArs Discovery instrument (NOMAD) is a spectrometer suite led by the Belgian Institute for Space Aeronomy (BIRA-IASB), being flown on the

ESA/Roscosmos ExoMars Trace Gas Orbiter mission. NOMAD is predominantly based upon the solar occultations in the infrared (SOIR) channel in the spectroscopy for the investigation of the composition of the atmosphere of Venus

instrument from the highly successful Venus Express mission, a compact high-resolution echelle grating spectrometer with an acousto-optical tunable filter for the infrared domain between 2.3 and 4.3  $\mu\text{m}$  [1–4].

NOMAD consists of three separate channels, solar occultation (SO), limb nadir and occultation (LNO), and ultraviolet and visible spectrometer (UVIS), all controlled via a single main electronics interface. SO and LNO are the infrared spectrometers which form the subject of this paper. UVIS is addressed in the companion paper to this article [5].

The SO channel has exactly the same optical design as SOIR, an infrared echelle-acousto-optical tunable filter (AOTF) spectrometer in the 2.3 to 4.3  $\mu\text{m}$  range with a resolving power at midrange of approximately  $\lambda/\Delta\lambda = 20,000$ , using uniquely the SO observation technique. It was proven during the Venus Express mission that, although SOIR does a great job as a SO instrument, its signal-to-noise ratio (SNR) is too low when observing at the limb or nadir. The contribution of thermal background in SOIR's wavelength domain drowns the weaker signal.

The LNO channel is similar to the SO channel but it has been optimized for observing weak IR light sources as encountered when observing Mars in the nadir or the limb. LNO has a reduced wavelength range (between 2.3 and 3.8  $\mu\text{m}$ ) and a resolving power at midrange of approximately  $\lambda/\Delta\lambda = 10,000$ .

The UVIS channel is an ultraviolet-visible spectrometer, capable of observations in both SO and nadir viewing geometries. UVIS is based upon the instrument designed and developed by the Open University, UK, for the ExoMars lander mission as part of the Humboldt payload [6]. UVIS operates over a wavelength range of 200 nm in the ultraviolet up to 650 nm in the visible, with a spectral resolution of approximately 1.5 nm. The UVIS channel is based on a Czerny-Turner layout, a totally different spectrometer concept than the infrared channels. Dual front-end telescopic viewing optics permit both viewing geometries to be achieved with a single spectrometer.

NOMAD's scientific goals are to look for trace gases of potential biological origin in the Martian atmosphere, identify potential source regions, and provide information on the nature of the processes involved. NOMAD will study the major climatological cycles, such as water, ozone and carbon cycles, the components and isotopes involved, and provide insight into their escape from the atmosphere. NOMAD will also look for traces of active geology and volcanism on Mars. Consequently the three key science objectives for NOMAD have been defined as follows.

Determine the trace gas composition of the Martian atmosphere by detecting species such as CO<sub>2</sub>, CO, H<sub>2</sub>O, HO<sub>2</sub>, NO<sub>2</sub>, N<sub>2</sub>O, CH<sub>4</sub>, C<sub>2</sub>H<sub>2</sub>, C<sub>2</sub>H<sub>4</sub>, C<sub>2</sub>H<sub>6</sub>, H<sub>2</sub>CO, HCN, H<sub>2</sub>S, OCS, HCl (SO and LNO channels), and SO<sub>2</sub>, O<sub>3</sub> (UVIS channel), and isotopes, such as <sup>13</sup>CO<sub>2</sub>, <sup>17</sup>OCO, <sup>18</sup>OCO, C<sup>18</sup>O<sub>2</sub>, <sup>13</sup>CO, C<sup>18</sup>O, HDO, <sup>13</sup>CH<sub>4</sub>, CH<sub>3</sub>D, not only in the lower and middle atmosphere, but also in the upper atmosphere. Contribute to the comprehension of the past and future evolution of the atmosphere by studying the upper atmosphere escape processes. Constrain the sources and sinks of methane, and study gases that relate to ongoing geophysical and volcanic activity.

For the above-mentioned trace gases, characterize their spatial and temporal variations. Refine the present knowledge of CO<sub>2</sub>--, CO-, H<sub>2</sub>O-, and O<sub>3</sub>- climatologies, and in general of atmospheric dynamics.

For the above-mentioned trace gases, characterize their production and loss mechanisms, and localize their sources. Refine the present knowledge of water, carbon, ozone and dust cycles, and their relation to surface mineralogy and polar ice formation.

The detailed science objectives of NOMAD are described in a separate paper [7].

## 2. DESIGN OBJECTIVES FOR SO AND LNO

### A. General Design Rules

The ExoMars trace gas orbiter (TGO) is a nadir tracking spacecraft, meaning that its -Y axis is always pointing toward and perpendicular to the surface of Mars. NOMAD has two nadir lines of sight (one in the LNO and one in the UVIS channel) that are parallel to this axis. Therefore, NOMAD's nadir viewports are always directed to Mars. The orbital configuration of ExoMars fixes the angle between its -Y axis and the direction of the Martian limb to 67.07° away from the -Y axis in the -Y/-X plane. NOMAD's three solar lines of sight (one in each of the channels) will be parallel to this limb direction, and hence form an angle of 67.07° with the nadir lines of sight. To perform SO measurements, the S/C will need to yaw rotate around its Y axis twice per orbit, once during the day, once during the night, so that, well before sunrise or sunset, the solar lines of sight point to the limb. During SOs the spacecraft will adopt an inertial pointing mode, fixed on the center of the Sun, resulting in an apparent ingress into or egress from the Martian disk. The TGO is therefore naturally suited to perform nadir and limb observations, and additionally offers the possibility to measure during SOs, when NOMAD's solar lines of sight pass through the atmosphere just before sunset or just after sunrise (Fig. 1).

To fulfill NOMAD's science goals during SOs, the SO, LNO, and UVIS channels must observe as similar a slice of the atmosphere as possible. To maximize the signal, the SO and LNO channel fields of view (FOV) must comprise the entire solar disc and the UVIS channel FOV must be as central as possible on the Sun. Therefore a good coalignment between the three channels shall be assured throughout the lifetime of the instrument (Fig. 2). It is required that each of the solar lines of sight is aligned to the instrument's mechanical axis with an accuracy of  $\leq \pm 0.15$  mrad. During nadir observations the footprints of the LNO and UVIS FOV overlap entirely, requiring an alignment accuracy with the mechanical axis of  $\leq \pm 10$  mrad.

Together with the NOMAD-to-spacecraft coalignment accuracy ( $\leq \pm 0.2$  mrad), the above-mentioned internal coalignment accuracies contribute to the overall pointing budget for NOMAD. Table 1 gives an overview of the requirements for the most important coalignment contributions, while Table 2 gives an overview of the requirements for the absolute and relative pointing errors.

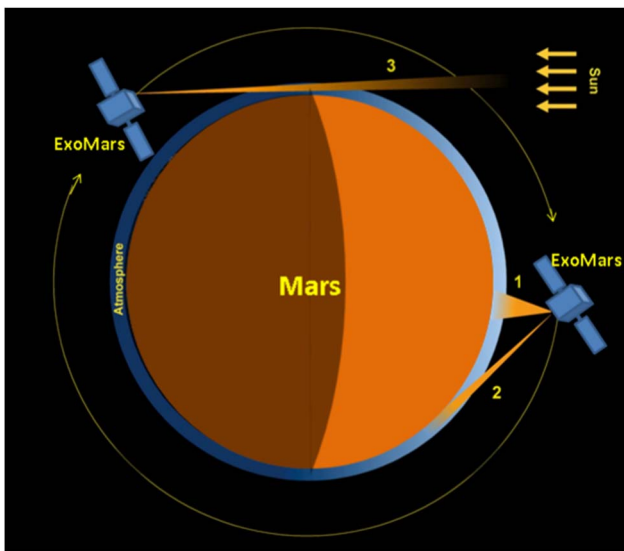


**Fig. 1.** Different observation modes with NOMAD in orbit around Mars (1 = nadir, 2 = limb, 3 = SO).

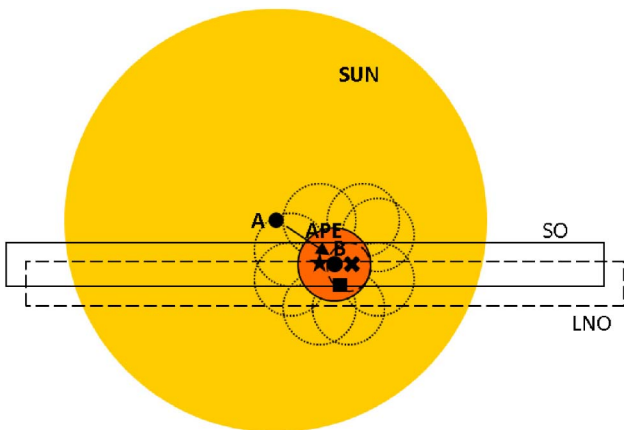


**Fig. 2.** NOMAD channel coalignment [A is center of the Sun; B is pointing axis of spacecraft; APE is absolute pointing error; full line rectangle is SO FOV; star is SO LOS; dashed line rectangle is LNO FOV; square is LNO LOS; dashed line circle is UVIS FOV; X is UVIS LOS; full line circle is maximum allowed misalignment between all LOS (including ACS); dotted targets are maximum allowed spacecraft RPE].

It is important to note that the rectangular FOV of the SO and the LNO channels shall be aligned by the spacecraft perpendicular to the limb at a chosen altitude above the surface (Fig. 3).

Since LNO's entrance aperture diameter is bigger, all its optical elements are larger. The height above the optical bench of the SO and LNO channels is 118 and 136 mm, respectively. Note also that additional external primary mirrors (periscopes) are needed to fold the solar lines of sight of SO, LNO, and UVIS into the direction of the Sun ( $67.07^\circ$ ).

The mass of NOMAD is 28.86 kg including margins. From this, the SO and LNO optical bench masses are 13.35 kg (including all NOMAD electronics) resp 9.4 kg. The remaining mass is attributed to UVIS (940 g) and harnessing, multilayer

**Table 1. Coalignment Contributors**

Coalignment Contributors	Accuracy Limit	Knowledge Accuracy
Solar LOS to NOMAD mechanical axis	$\pm 0.15$ mrad	
Nadir LOS to NOMAD mechanical axis	$\pm 10.0$ mrad	
NOMAD mechanical axis to spacecraft axis	$\pm 0.20$ mrad	0.05 mrad
Any NOMAD solar LOS to spacecraft axis <sup>a</sup>	$\pm 0.30$ mrad	

<sup>a</sup>It is assumed that the ACS instrument, which performs SO measurements at the same time as NOMAD, has a similar coalignment budget of  $\pm 0.30$  mrad, leading to a maximum misalignment between the NOMAD and ACS solar lines of sight of 0.60 mrad.

**Table 2. Pointing Budget**

Pointing	Error Limit	Knowledge Accuracy
Absolute pointing error (APE) solar	$\leq 1.23$ mrad	
Relative pointing error (RPE) solar (short + long term) <sup>a</sup>	$\leq 1.23$ mrad	
Absolute pointing error (APE) nadir	$\leq 3.50$ mrad	
Relative pointing error (RPE) nadir (long term) <sup>a</sup>	$\leq 3.00$ mrad	
Relative pointing error (RPE) nadir (short term) <sup>a</sup>	$\leq 0.54$ mrad	
Overall pointing knowledge solar		$\leq 0.45$ mrad
Overall pointing knowledge nadir		$\leq 0.54$ mrad

<sup>a</sup>Short term is 1 s, long term is 60 s.

insulation (MLI), and instrument-to-spacecraft mounting hardware (3.7 kg).

NOMAD has to survive in the environmental conditions imposed by the spacecraft. The most severe constraints are the operational ( $-30^\circ\text{C}$  to  $+50^\circ\text{C}$ ) and nonoperational ( $-40^\circ\text{C}$  to  $+60^\circ\text{C}$ ) thermal limits.

## B. SO Channel

Since the SO channel of NOMAD builds strongly on the heritage of SOIR, its design objectives are kept unchanged. The

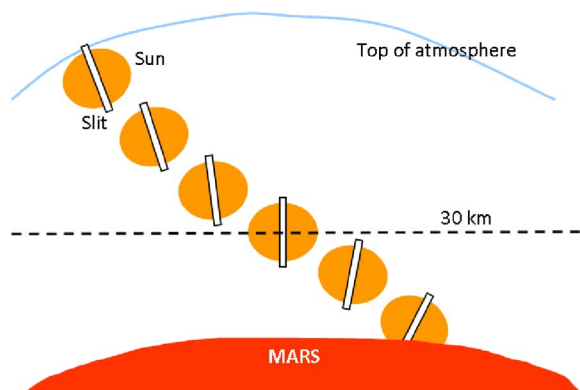


**Fig. 3.** Example of slit orientation in Mars atmosphere (slit perpendicular to limb at 100 km altitude).

principle of combining an AOTF as an order sorter and an echelle grating spectrometer are not put in cause. The spectral observation band covers the 2.3 to 4.3  $\mu\text{m}$  range, the instrument line profile (ILP) is 0.22  $\text{cm}^{-1}$  full width at half-maximum (FWHM) or better over the whole spectral range, to be sampled by at least two detector pixels. Given the importance of detecting methane (absorption line around 3000  $\text{cm}^{-1}$ ), the instrument is optimized close to that wavenumber, resulting in an ILP of 0.15  $\text{cm}^{-1}$  FWHM at 3.3  $\mu\text{m}$ .

The FOV of the SO channel is driven by the fact that it has to observe solely during SO. The SOIR FOV for the spatial dimension of 30 arcmin is maintained although the maximum apparent diameter of the Sun at Mars is considerably smaller (23 arcmin) compared to Venus (44 arcmin). It is required that all the detector lines illuminated by the solar disk can be downloaded to Earth. Perpendicular to the spatial direction a FOV of 2 arcmin is maintained resulting in sufficient height resolution while vertically scanning through the Martian atmosphere (vertical sampling  $\leq 1$  km). From dimensional constraints it follows that the entrance aperture diameter of the SO channel shall be at maximum 20 mm.

SO has a SNR  $\geq 900$  over the complete spectral range, measured over a zone of 200 detector columns centered on the column with the maximum signal, for a minimum solar signal (i.e., at maximum Mars–Sun distance) and including all instrument sources of noise. Table 3 gives an overview of the characteristics of the SO channel.

### C. LNO Channel

For LNO operating in SO mode, the same design objectives are valid as for the SO channel. It is clear that the most challenging design objectives are situated in the nadir and limb mode of this channel, where much weaker signal input is seen. Maintaining sufficient SNR is the main design driver here. The channel has an SNR of  $\geq 400$  over the complete spectral domain, after binning of all detector rows by column, measured over a zone of 200 columns centered on the column with the maximum signal, for a minimum solar signal (i.e., at maximum Mars–Sun distance), and including all instrument sources of noise. In the

**Table 3. Summary of SO Channel Specifications**

Characteristic	Value or Range	Unit
Wavelength $\lambda$	2.3–4.3	$\mu\text{m}$
Wavenumber	4250–2320	$\text{cm}^{-1}$
Instrument line profile (ILP)	0.22	$\text{cm}^{-1}$
ILP for $\text{CH}_4$	0.15	$\text{cm}^{-1}$
Pixel sampling (FWHM)	$\geq 2$	
Polarization	linear, parallel to slit	
Resolving power $\lambda/\Delta\lambda$	20,000	
Slit width in object space	2	arcmin
Slit length in object space	30	arcmin
Field of view	2 $\times$ 30	arcmin
Spatial sampling	1	arcmin
Vertical sampling	$\leq 1$	km
SNR	$\geq 900$	
Mass (incl all NOMAD electronics)	13.5	kg
Dimensions (without periscope)	490.5 $\times$ 353 $\times$ 208	$\text{mm}^3$

region that contains the methane absorption line, LNO has an SNR of  $\geq 1000$ .

As a price to pay for the challenging SNR specification, the wavelength range (between 2.3 and 3.8  $\mu\text{m}$ ) and ILP (0.5  $\text{cm}^{-1}$ , sampled by at least two pixels) are reduced in comparison with SO.

While defining an appropriate instantaneous FOV for the LNO channel, a compromise had to be found between the channel performance in SO (vertical sampling) and in nadir mode (SNR, footprint). LNO has a FOV of 150  $\times$  4 arc min. With a spacecraft orbit altitude of 400 km, a line of sight (LOS) moving along track with a velocity of approximately 3 km/s, a variable orientation of the instantaneous FOV and a maximum measurement time of 15 s, the footprint of the LNO FOV on the Martian surface is never larger than 1° by 0.3° or 51 km by 17.5 km. Since LNO uses this FOV also for SOs, the vertical sampling capacity of LNO is reduced by a factor of 2 compared to the SO channel. The entrance aperture diameter of the LNO channel is nearly 30 mm, which is greater than that of the SO channel, to provide higher signal input. Table 4 gives an overview of the characteristics of the LNO channel.

Both in the SO and the LNO channel the presence of ghost peaks and stray light, as well as optical aberrations such as tilt, smile and frown, has been minimized as much as possible.

### 3. SPECTROMETER DESIGN OF THE INFRARED CHANNELS

With the above-mentioned design objectives and maximum maintenance of SOIR heritage as drivers, it was decided to build both infrared channels around a high-dispersion echelle grating. To avoid overlap of orders at the output of the grating, AOTFs, (manufactured by Gooch and Housego, UK) are

**Table 4. Summary of LNO Channel Specifications**

Characteristic	Value or Range	Unit
General		
Wavelength $\lambda$	2.3–3.8	$\mu\text{m}$
Wavenumber	4250–2630	$\text{cm}^{-1}$
Instrument line profile (ILP)	0.5	$\text{cm}^{-1}$
Pixel sampling (FWHM)	$\geq 2$	
Polarization	linear, parallel to slit	
Resolving power $\lambda/\Delta\lambda$	10,000	
Slit width in object space	4	arcmin
Slit length in object space	150	arcmin
Field of view	4 $\times$ 150	arcmin
Spatial sampling	1	arcmin
Entrance aperture diameter	29.5 $\times$ 24	$\text{mm}^2$
Mass	9.4	kg
Dimensions (without periscope)	445 $\times$ 327 $\times$ 182	$\text{mm}^3$
SOs		
Vertical sampling	$\leq 1$	km
SNR	$\geq 900$	
Nadir		
Footprint (400 km orbit)	60 $\times$ 0.3	$\text{km}^2$
	60 $\times$ 17.5	
SNR	$\geq 400$	
SNR for $\text{CH}_4$	$\geq 1000$	

placed as order sorting devices in front of the spectrometer sections. We remind that the use of echelle gratings has the distinct advantage over other types of spectrometers (based, e.g., on cross-orthogonal dispersion) that the full height of the detector can be used to register spectral lines, allowing to improve the SNR by column binning. AOTFs, on the other hand, offer a quick electronic driven random access to the spectral orders, with no need for moving mechanical parts, and with the possibility to use them as an optical shutter, blocking incident light so that background measurements can be performed.

The optical principle, which is valid for the two channels, is given in Fig. 4. The real optical layout of SO and LNO is shown in Figs. 5 and 6, respectively. The front-end optics of the channels consists of the AOTF entrance optics (nr.3) that is a telescope matching the incoming light beam to the acceptance angle of the AOTF. In the intermediate image plane of the entrance optics a diaphragm (nr.4) is placed that limits the FOV

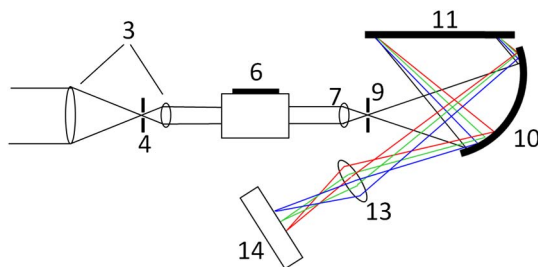


**Fig. 4.** Optical principle of NOMAD's infrared channels channel.

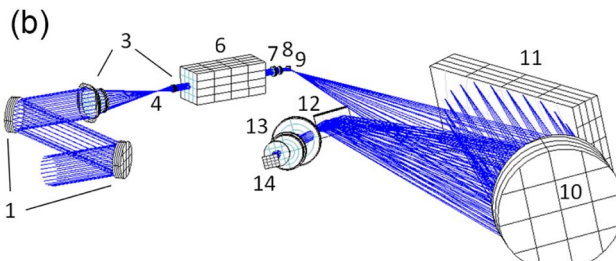
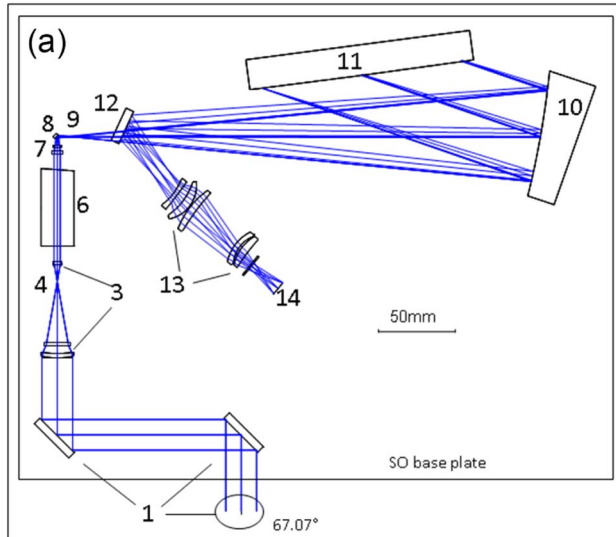


**Fig. 5.** Optical design of the SO channel: (a) 2D and (b) 3D.

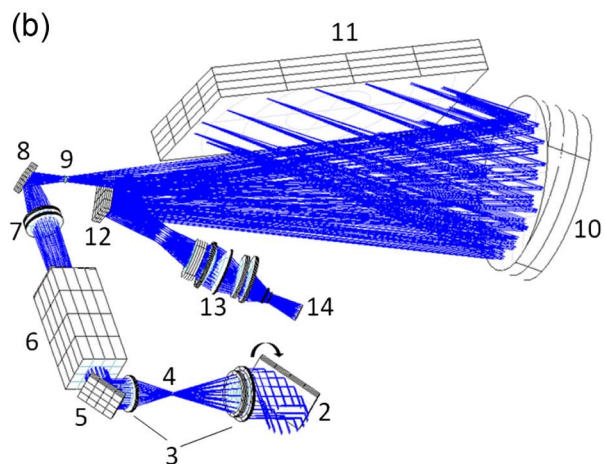
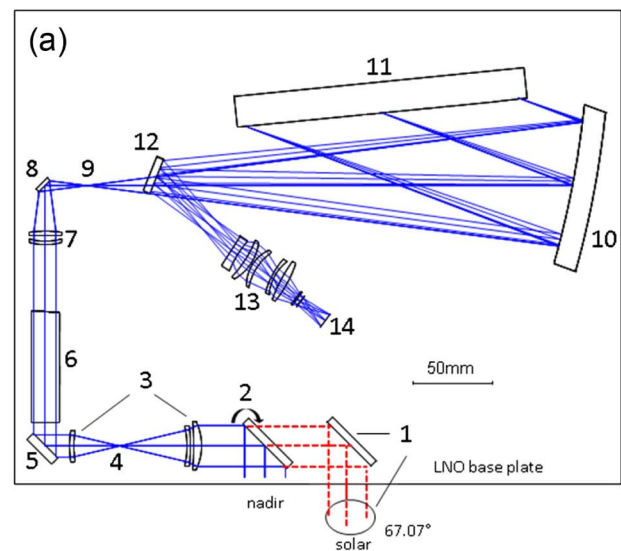


**Fig. 6.** Optical design of the LNO channel: (a) 2D top and (b) 3D bottom.

of the system in order to reduce scattering and ghost images, and to prevent overlap between order 1 and order 0 of the AOTF. In the LNO channel an additional folding mirror (nr.5) had to be inserted between AOTF entrance optics and the AOTF. An AOTF (nr.6) selects the order from the incoming light beam that corresponds to an RF signal applied to the crystal, and outputs this small fraction of the beam toward the AOTF exit optics (nr.7). All other orders are blocked. Via a small folding mirror (nr.8) the AOTF exit optics creates an image of the scene (Sun or surface of Mars) on the spectrometer entrance slit (nr.9). The slit defines the FOV of the spectrometer. An off-axis parabolic mirror (nr.10) serves as a collimating lens in the spectrometer section and offers a parallel light beam to the echelle grating (nr.11). After dispersion of the light by the grating, the beam passes again by the parabolic mirror (nr.10), now serving, together with the detector optics (nr.13), as an imaging lens. Via a folding mirror (nr.12) the beam is projected on the detector (nr.14) that has its optical axis parallel to the overall optical axis of the channel. The spectral properties of the channels [free spectral range (FSR), instrument line profile] are accomplished by the choice of the configuration and

characteristics of echelle grating, parabolic mirror, and detector optics. To obtain the required spectral sampling interval of the system, also the pixel size of the detector is of importance.

The entrance of the SO channel is a periscope consisting of three flat mirrors (nr.1 in Fig. 5). The two mirrors inside the SO base plate are needed to shift the channel's aperture to a location where the incoming beam is not obstructed by other spacecraft elements. The third mirror is protruding outside the base plate and tilts the optical axis by 67.07° in the direction of the Martian limb.

The LNO channel has two entrance apertures. The solar entrance is a periscope with two flat mirrors (nr.1 in Fig. 6), one inside the base plate, one protruding and tilting the beam by 67.07°. The nadir entrance consists of one single flat flip mirror (nr.2). This mirror is driven by a motor and can be placed either inside the beam (nominal position, the LNO channel looks at the nadir) or outside the beam (the LNO channel looks at the Sun).

Although the conceptual design of the SO and LNO channels is similar, some differences can be noticed. In the SO channel, from heritage, the *F*-numbers of the optics ( $f/5.16$ ) and the detector ( $f/3.936$ ) are not matched; in LNO they are  $f/3.936$  everywhere. While the focal length (103 mm) remains the same in the two channels, this means that the optical elements in LNO scale up in size by approximately 30%, and a higher spectrometer slit can be used, contributing positively to the SNR (see below).

In the SO channel the limiting aperture of the system is the diaphragm in the AOTF entrance optics ( $f/\# = f/5.16$ ), while in the LNO channel it is the cold shield of the detector ( $f/\# = f/3.936$ ). This means that in SO it is the entrance pupil (coincident with the first lens of the instrument) that is imaged along the optical path, and in LNO it is the exit pupil (coincident with the cold shield). Images of the respective pupils are formed at the first lens and the cold shield, but also at two other positions in the instrument: (1) in the middle of the AOTF to avoid vignetting of the spatial FOV at the entrance and exit of the crystal; and (2) on the grating, to keep its dimensions as small as possible. Table 5 gives an overview of the first-order optical properties for the two channels.

#### 4. GRATING AND IMAGER OPTICAL PROPERTIES

##### A. Free Spectral Range

For an echelle grating that is used in the Littrow configuration (incidence angle  $\alpha$  and diffraction angle  $\beta$  are the same and equal to the blaze angle  $\Theta_B$ ) the grating equation is [8,9]

$$m \cdot \lambda_c = \frac{\sin \alpha + \sin \beta}{g} = \frac{2 \cdot \sin \theta_B}{g}, \quad (1)$$

where  $g$  is the groove density (in lines/mm) of the grating,  $m$  the diffraction order, and  $\lambda_c$  the central wavelength of order  $m$ .

The echelle gratings in the infrared channels of NOMAD are used in a "near" Littrow configuration. To separate the incident and diffracted beam, the gratings are slightly tilted such that both beams make a small angle  $\gamma$  with the plane that is perpendicular to the grating surface and the grooves. Besides that there is also a small deviation  $i$  of the angle of incidence

**Table 5. First-Order Optical Properties**

Parameter	SO	LNO	Unit
Entrance aperture	$20 \times 20$ (circular)	$29.5 \times 24$ (elliptical)	mm <sup>2</sup>
Overall focal length	103		mm
Focal length optics in front of slit	103		mm
Magnification AOTF entrance optics	5×	1.85×	
Focal length AOTF "objective"	58.4	57.0	mm
Focal length AOTF "collimator"	11.6	30.7	mm
Focal length AOTF exit optics	20	55.8	mm
Magnification optics behind slit		1×	
Focal length collimating lens	300		mm
Focal length imaging lens	300		mm
Focal length parabolic mirror	300		mm
Magnification detector optics		1×	
Limiting <i>F</i> -number	$f/5.12$	$f/3.936$	

from the blaze angle in the plane normal to grooves and surface. In these conditions the simplified grating Eq. (1) has to be re-written as

$$m \cdot \lambda_c = \frac{2 \cdot \sin \theta_B \cdot \cos i \cdot \cos \gamma}{g}. \quad (2)$$

The spectrometer design and alignment of the NOMAD channels is such that the central wavelength  $\lambda_c$  of each order falls in the center of the detector.

The FSR, the wavelength range in which there is no overlap by adjacent orders, is a constant for echelle gratings:

$$\text{FSR} = \frac{1}{\lambda_c \cdot m} = \frac{g}{2 \cdot \sin \theta_B \cdot \cos i \cdot \cos \gamma} = Cte. \quad (3)$$

The wavelengths at the edges of the FSR can be derived from Eqs. (2) and (3) as follows:

$$\lambda_0 = \lambda_c \pm \frac{\text{FSR}}{2} = \frac{2 \cdot \sin \theta_B \cdot \cos i \cdot \cos \gamma}{g \cdot (m \pm 1/2)}. \quad (4)$$

Table 6 gives an overview of the grating characteristics. Tables 7 and 8 give for each channel the theoretical values of  $\lambda_c$ ,  $\lambda_0^+$ , and  $\lambda_0^-$  for some orders.

Writing again the grating Eq. (2) for the near-Littrow case of NOMAD, now for a diffracted beam at wavelength  $\lambda$ , making an angle  $\phi$  with the diffracted ray at wavelength  $\lambda_c$ , the ray that defines the optical axis of the imager, we have

$$m \cdot \lambda = \frac{[\sin(\theta_B + i) + \sin(\theta_B - i - \phi)] \cdot \cos \gamma}{g}. \quad (5)$$

A special case of Eq. (5) can be written for the rays at wavelengths  $\lambda_e^+$  and  $\lambda_e^-$  that fall on the edges of the detector's sensitive area:

$$m \cdot \lambda_e^+ = \frac{[\sin(\theta_B + i) + \sin(\theta_B - i + \Delta\varphi)] \cdot \cos \gamma}{g} \quad (6)$$

**Table 6.** Grating Characteristics

Parameter	SO	LNO	Accuracy	Unit
Wavelength range	2.3–4.3	2.3–3.9		μm
Blaze angle $\Theta_B$		63.43	±0.1	°
Groove density $g$ (at 24.5°C) <sup>a</sup>		4.031283		lines/mm
Groove density $g$ (at 0°C) <sup>b</sup>		4.033512		lines/mm
Total number of grooves on grating $N$	≥593	≥765		
Groove spacing (at 24.5°C) <sup>a</sup>		248.06	±0.001	μm
Length of grooved area		$N \times 248.06$	±0.1	μm
Off Littrow angle $\gamma$	2.6	2.75	±0.025	°
Off blaze angle $i$	-0.02	0	±0.016	°
Useful area	≥147.1 × 74.5	≥ 190 × (97.50–91.85) <sup>c</sup>		mm <sup>2</sup>
Size ( $L \times W \times T$ )	148.1 × 96.84 × 25	191 × 123.5 × 40	±0.1	mm <sup>3</sup>
Free spectral range FSR	22.56			cm <sup>-1</sup>
Efficiency at near-Littrow condition <sup>d</sup>	85	85	2	%

<sup>a</sup>Manufacturing temperature.<sup>b</sup>Goal operating temperature.<sup>c</sup>Useful area is not fully rectangular.<sup>d</sup>Drops to approximately half the value at grating edges.**Table 7.** Theoretical Values for  $\lambda_c$ ,  $\lambda_0^+$ ,  $\lambda_0^-$ ,  $\lambda_e^+$ ,  $\lambda_e^-$ , and the Dispersion on the Detector at  $\lambda_c$  for SO

Order	$\lambda_c$ [μm]	$\lambda_0^+$ [μm]	$\lambda_0^-$ [μm]	$\lambda_e^-$ [μm]	$\lambda_e^+$ [μm]	$\partial\lambda/\partial D$ [cm <sup>-1</sup> /mm]
100	4.4302	4.4082	4.4524	4.4123	4.4477	1.88
110	4.0275	4.0093	4.0459	4.0112	4.0434	2.07
120	3.6919	3.6765	3.7073	3.6770	3.7064	2.25
130	3.4079	3.3948	3.4210	3.3941	3.4213	2.44
140	3.1661	3.1532	3.1758	3.1517	3.1769	2.63
150	2.9535	2.9437	2.9637	2.9416	2.9651	2.82
160	2.7689	2.7603	2.7776	2.7577	2.7798	3.01
170	2.6060	2.5984	2.6137	2.5955	2.6163	3.19
180	2.4612	2.4544	2.4681	2.4513	2.4709	3.38
190	2.3317	2.3256	2.3379	2.3223	2.3409	3.57
200	2.2151	2.2096	2.2207	2.2062	2.2239	3.76

and

$$m \cdot \lambda_e^- = \frac{[\sin(\theta_B + i) + \sin(\theta_B - i - \Delta\varphi)] \cdot \cos \gamma}{g}. \quad (7)$$

Tables 7 and 8 give for each channel the values of  $\lambda_e^+$  and  $\lambda_e^-$  for some orders. The product of the order and the wavelength at a given pixel, e.g., the central pixel or the two edge pixels, in the “near”-Littrow condition, remains “nearly” constant throughout the complete spectral domain.

It has to be noted that the free spectral range of the NOMAD channels (FSR = 22.56 cm<sup>-1</sup>) is slightly larger than the spectral span of the detector’s sensitive area for lower orders.

There the edges of the free spectral range that fall off the detector. For orders  $m = 130$  and higher, the free spectral range falls entirely on the detector.

### B. Dispersion and Spectral Sampling Interval

Also the spectral sampling interval on the detector is defined by the grating characteristics.

By differentiating Eq. (5) we obtain

$$\frac{g \cdot m}{\cos \gamma} \cdot \partial\lambda = \cos(\theta_B - i - \varphi) \cdot \partial\varphi. \quad (8)$$

While wavelength  $\lambda_c$  is forced to fall in the center of the detector, wavelength  $\lambda$  falls a distance  $D$  away from the center of the detector,

**Table 8.** Theoretical Values for  $\lambda_c$ ,  $\lambda_0^+$ ,  $\lambda_0^-$ ,  $\lambda_e^+$ ,  $\lambda_e^-$ , and the Dispersion on the Detector at  $\lambda_c$  for LNO

Order	$\lambda_c$ [μm]	$\lambda_0^+$ [μm]	$\lambda_0^-$ [μm]	$\lambda_e^-$ [μm]	$\lambda_e^+$ [μm]	$\partial\lambda/\partial D$ [cm <sup>-1</sup> /mm]
120	3.6914	3.6761	3.7069	3.6765	3.7059	2.26
130	3.4076	3.3944	3.4206	3.3937	3.4208	2.44
140	3.1641	3.1528	3.1754	3.1513	3.1765	2.63
150	2.9531	2.9433	2.9630	2.9412	2.9647	2.82
160	2.7686	2.7599	2.7772	2.7574	2.7794	3.01
170	2.6057	2.5980	2.6134	2.5952	2.6159	3.20
180	2.4609	2.4541	2.4678	2.4510	2.4706	3.39
190	2.3314	2.3253	2.3376	2.3220	2.3406	3.57
200	2.2148	2.2093	2.2204	2.2059	2.2235	3.76

$$D = f_{\text{imager}} \cdot \tan \varphi, \quad (9)$$

where  $f_{\text{imager}}$  is the focal length of the imaging system. After differentiation of this equation we have

$$\partial D = \frac{f_{\text{imager}}}{\cos^2 \varphi} \cdot \partial \varphi. \quad (10)$$

Combining Eqs. (8) and (10) the dispersion  $\partial \lambda / \partial D$ , which indicates how the light is spectrally spread over the detector, can be written as

$$\frac{\partial \lambda}{\partial D} = \frac{\cos^2 \varphi \cdot \cos(\theta_B - i - \varphi) \cdot \cos(\gamma)}{f_{\text{imager}} \cdot m \cdot g}. \quad (11)$$

Tables 7 and 8 give for both channels the dispersion for the central wavelengths  $\lambda_c$ , for some orders, expressed in  $\text{cm}^{-1}$  per mm. Knowing the width of the detector pixels in the spectral direction, the spectral sampling interval can be easily calculated (see below). The value of the focal length of the imager  $f_{\text{imager}}$  is a compromise value resulting in the best possible spectral sampling over the complete wavelength range.

### C. Imager Optics

The imager optics in NOMAD's infrared channels consists of three elements (see Fig. 7): (1) a focusing off-axis parabolic mirror; (2) a flat mirror that bends the light path in order to stay within the dimensional constraints of the instrument; and (3) a lens module called detector optics. As mentioned earlier, the parabolic mirror has a double use. It serves as a collimator for the light that goes toward the grating, and as an imager for the light that reflects from it. In both channels this mirror has a focal length of 300 mm and is used off-axis, 19° in SO and 20.75° in LNO. The light is partly reflected out of the horizontal plane, in SO by 1.46°, in LNO by 1.75°. The detector optics image the entrance pupil and the grating on the cold shield of the detector. They project the image formed by the parabolic mirror on the detector with 1x magnification. The lenses used in the module are spherical. To compensate for

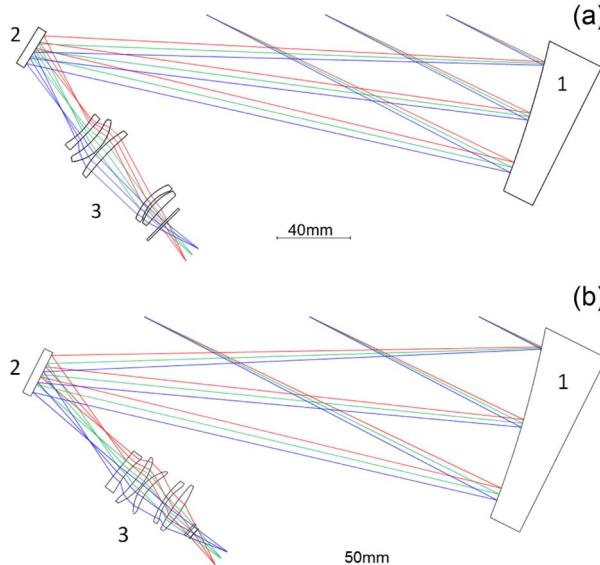


**Fig. 7.** Optical layout of imager: (a) SO channel and (b) LNO channel.

the aberrations of the parabolic mirror the module is divided in two lens groups that are both tilted and decentered. In SO the lenses are made of Ge, ZnSe, Si, Ge and Si, respectively, with clear apertures varying between 20 and 30.5 mm. In LNO the lens materials are Ge, Si, ZnSe, Ge and Si, respectively, with clear apertures between 22.1 and 28.2 mm.

### D. Manufacturing and Verification of Gratings

Worldwide only a few companies are capable of manufacturing low-groove-density large-area gratings with high enough precision [10]. In Table 6 it is seen that stringent accuracies are imposed on crucial grating parameters. Especially the accuracy on the groove-to-groove distance ( $\pm 1$  nm) over the total groove height is challenging. This high pitch accuracy is needed to get usable wavefronts, but not easy to achieve due to high tool load and consequent elastic deformations during the ruling process.

Not only the echelle groove pitch needs to be very precise, also the quality (flatness/roughness) of the groove facets is of utmost importance as well as the overall flatness of the grating. Following the DIN3140 standard, the grating surface should have at maximum 0.5 fringes over the total length of the grating (deviation requirement), with at maximum 0.25 fringes difference between two perpendicular directions on the surface (irregularity requirement). Additionally the RMS surface error, measured in reflection, has to be  $\leq \lambda/15$ , and the slope error  $\leq 0.1$  mrad. All these requirements are valid at a verification wavelength of 547 nm. The NOMAD grating is manufactured at AMOS, Belgium.

The NOMAD gratings and their mechanical support are monolithic, manufactured from one block of 6061-T6 aluminum alloy with hollowed honeycomb back. This results in a non-negligible mass reduction of approximately 20%, it avoids a delicate grating-to-holder gluing process and assures a more homogeneous thermal distribution. The block passed through a double heat treatment for stress relief and stabilization of the substrate, before diamond machining was started. All nonruled surfaces of the grating underwent a protective chromate passivation conversion (Alodine-1200 coating) while the echelle grooves received first a 20 nm thick Cr transition coating, followed by a final 300 nm thick Au coating (CSL, Belgium).

In order to avoid scattering of light on the adjacent surfaces of the grooves and in the bottom corners (due to rounding by the tip radius  $R$  of the manufacturing tool), the angle between the reflective surface and the adjacent surface is not 90°, but lowered by a maximum of 6° (Fig. 8).

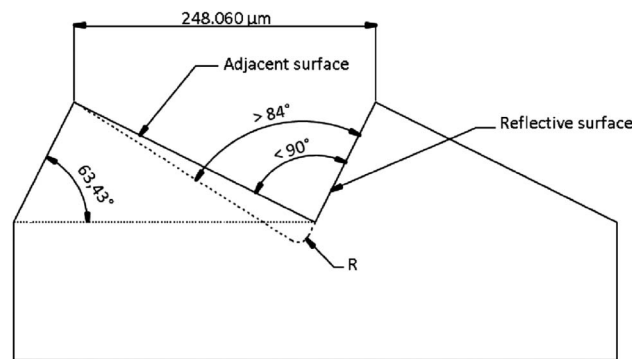


**Fig. 8.** Grating section with slightly over-tilted adjacent surfaces.

For alignment purposes the grating body is foreseen with two mirroring surfaces. Their position has to be known with respect to the reference plane of the grating with an accuracy of 10 arcsec. The mirrors have a reflectivity of  $\geq 70\%$  for visible light and a flatness  $\leq \lambda/2$  at 632.8 nm.

AMOS produced gratings that, after verification with visible light at 632.8 nm on a laser ZYGO Verifire (for SO) and an RTI 4100 WYKO (for LNO) interferometer through a density pellicle, show full compliance to the surface quality specifications. A comparative test has been performed after delivery of the gratings in order to assess their spectral performance, especially the appearance of unwanted ghost peaks, and their efficiency. The flight spare model of SOIR was used as test setup, first with a SOIR grating, then with the new NOMAD grating (Fig. 9). A laser line at 3.39  $\mu\text{m}$  was guided through the system. While on the SOIR grating a clear ghost peak can be distinguished, the NOMAD grating remained free of ghosts. It can also be seen that the NOMAD grating is twice as efficient as the SOIR grating (comparison of the relative main peak intensity). On the other hand the main peak is broader on the NOMAD grating. This last effect can be completely corrected by a detector refocusing.

On samples, representative for the applied Cr-Au-coating, a thermal-vacuum, an humidity, an adhesion, and an abrasion test were successfully performed. In Fig. 10 pictures of the SO and LNO gratings are shown.

### E. Manufacturing and Verification of Parabolic Mirrors

Like the gratings, the parabolic mirrors are also monolithic. They are manufactured by the University of Dundee and provided

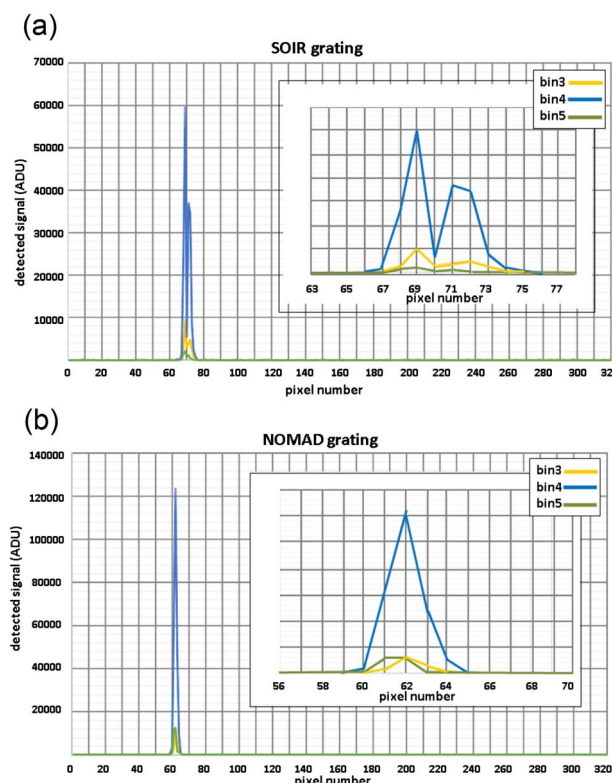


**Fig. 9.** Comparison between (a) SOIR and (b) NOMAD grating.

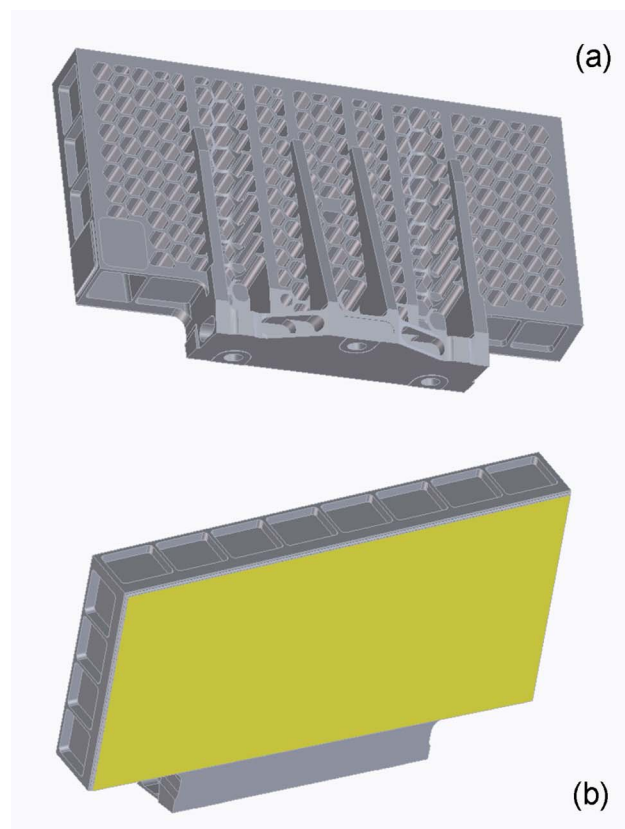


**Fig. 10.** Pictures of (a) SO-grating back and (b) LNO-grating front.

by Davin Optronics Ltd. (UK). Both the SO and the LNO mirrors have a conical surface with a radius of curvature of  $600 \pm 0.1$  mm, in SO used  $100 \pm 0.05$  mm off-axis and in LNO  $109.37 \pm 0.05$  mm off-axis. In SO the mirror has a clear aperture diameter of 80 mm and in LNO of 103.4 mm. Flat mirror alignment reference surfaces are located on the side and on the back of the parts. The back side of the mirror is hollowed to save mass, but preserves at its contour a full flat back reference surface used during machining. The mirror is rough-manufactured from a block of RSA-6061 aluminum by conventional machining, followed by a thermal treatment for stress relief. The mirror surface, reference mirror surfaces and mechanical interfaces are fine-manufactured by single point diamond turning, ensuring the imposed tolerances (e.g.,  $<1$  fringe at 632.8 nm surface irregularity and  $<30$  nm RMS surface roughness for the main mirror). The main mirror carries a protective SiO coating with an optical thickness of  $\lambda/2$  at 3000 nm. Figure 11 shows the parabolic mirrors for SO and LNO. All dimensions (radius of curvature, off-axis dimension, etc.) plus surface irregularity and roughness have been checked by optical metrology at the Precision Optics Laboratory of Durham University (UK).

### 5. AOTF CHARACTERISTICS AND AOTF OPTICS

#### A. Working Principle

An important characteristic of acousto-optical tunable filters is that the FWHM of their spectral band, expressed in

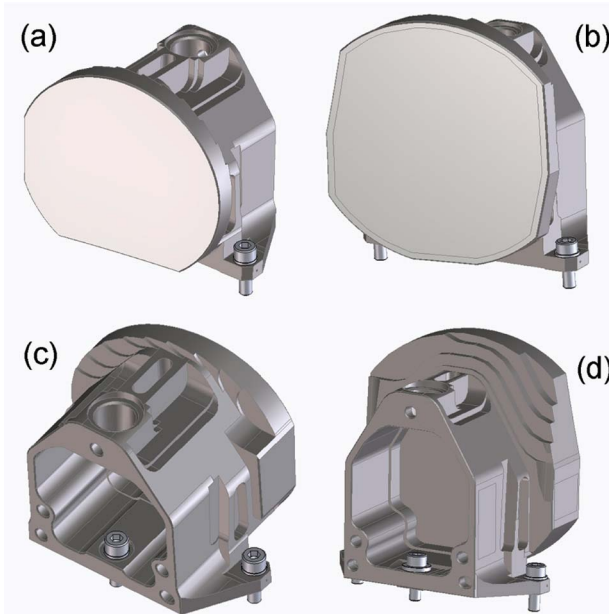


**Fig. 11.** Pictures of parabolic mirror front and rear side [(a),(c): SO; (b),(d): LNO].

wavenumber units, is more or less constant over the complete wavelength range with typical values between 22 and 25 cm<sup>-1</sup>. This means that the passband of the AOTFs can be nicely matched to the free spectral range of the gratings, resulting in an optimized system.

The NOMAD AOTFs are tetragonal crystals made of a birefringent material that is transparent in the applicable infrared domain. The working principle of an AOTF is based on Bragg diffraction [11,12], diffraction that occurs in crystalline structures when an acoustic wave interacts with optical waves. Part of the nonpolarized light entering the crystal travels to the exit of the AOTF without diffraction, part is diffracted at a small angle (diffraction angle, see Table 9) to either side of the undiffracted beam. Both the undiffracted and diffracted light beams contain an ordinary and an extraordinary polarization component, which exit the AOTF under slightly different angles. The plane of diffraction is the plane formed by the (110)- and (001)-crystal axes (see Fig. 12). In NOMAD only the ordinary polarization of the incoming light ( $k_o$ ) is used. In the AOTF the polarization plane rotates and hence, it is the extraordinary polarization of the diffracted light beam ( $k_e^*$ ) that is transferred toward the spectrometer.

The output face of the AOTF is slightly inclined with respect to the input face (angle between input and output plane, see Table 9). This oblique cut refolds the diffracted output beam in line with the optical axis of the channel. The unwanted undiffracted beam is clearly separated from the useful beam (by the diffraction angle) and is easily blocked.

### B. Tuning Curve

The acoustic waves, necessary to produce the Bragg diffraction, are injected through a transducer that is bonded to a long side face of the crystal. Electrical radio frequency waves are applied to the transducer and converted there in acoustic power. The central wavelength, expressed in wavenumbers, of the AOTF

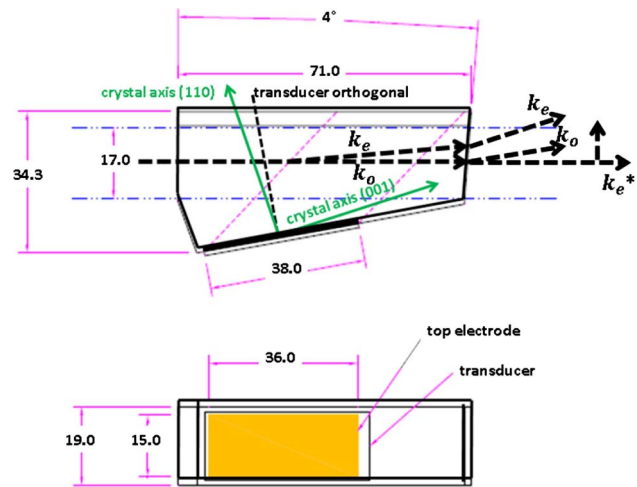


**Fig. 12.** Layout of LNO AOTF with indication of system axes and beam polarization ( $k_o$  and  $k_e$  are the incoming ordinary and extraordinary beams,  $k_e^*$  is the useful diffracted extraordinary beam).

passband is proportional to the applied radio frequency (between 14 and 30 MHz). This relationship is called the AOTF tuning curve. Both the radio frequency and the acoustic power are electrically tunable and hence controlled by NOMAD's

**Table 9. AOTF Characteristics for the SO and LNO Channel**

Parameter	SO	LNO	Unit
Material	TeO <sub>2</sub>		
Spectral bandwidth (FWHM)	22 ± 1	24 ± 1	cm <sup>-1</sup>
Spectral range	2.2–4.3	2.2–3.9	μm
Acceptance aperture in plane of diffraction	5	17	mm
Acceptance aperture perpendicular to plane of diffraction	5	15	mm
Acceptance angle in plane of diffraction	±3	≥ ± 2.15	°
Acceptance angle perpendicular to plane of diffraction	±3	≥ ± 2.15	°
Diffraction angle	4.2	5.2	°
Diffraction efficiency overall	≥50	≥80	%
Diffraction efficiency at 3.39 μm	≥60	≥80	%
Distance between input and output plane	50	71	mm
Angle between input and output plane	4.2	4.0	°
Sidelobe suppression (absolute)		-27	dB
Sidelobe suppression (% of main lobe)		4.5	%
RF frequency	14.20–28.00	15.95–29.83	MHz
Maximum available RF input power		2	W
Harmonic frequencies suppression (absolute)		-30	dB
Harmonic frequencies suppression (% of fundamental)		0.001	%

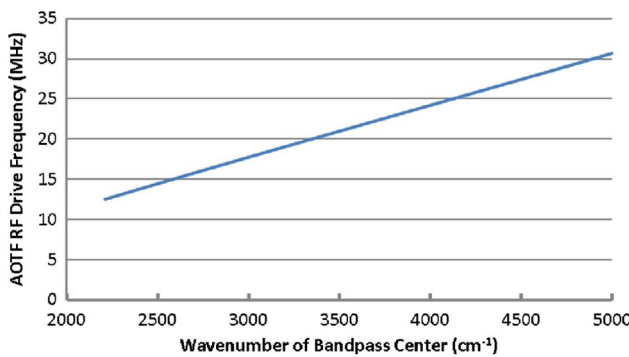


**Fig. 13.** Typical wavenumber to radio frequency tuning curve for the NOMAD SO AOTF at room temperature.

central electronics. An example of an AOTF tuning curve for SO is given in Fig. 13.

AOTF tuning curves are slightly temperature dependent. This is one of the intrinsic problems of using AOTFs in the infrared wavelength domain. To obtain good diffraction efficiency, nonnegligible power (several watts) has to be used, leading to thermal dissipation inside the crystal. Several mitigation solutions are applied in the design of the NOMAD AOTFs, and especially in the LNO AOTF, where, due to the faint input signal, the highest possible diffraction efficiency is required. One of the solutions is to use an AOTF and transducer that are as long as possible, such that the acousto-optical interaction length is maximized. While for SO the length of the crystal is 50 mm, for LNO a crystal with a length of over 70 mm is used, which is close to the technical limitations of growing pure  $\text{TeO}_2$  crystals. Also measures are taken for heat draining from the crystal. The overall NOMAD instrument power budget imposes a maximum allowable RF power of 2 W in the SO and the LNO AOTF.

### C. Sidelobes

When designing AOTFs and their driving electronics, attention should be paid to avoid “pollution” of the main passband through leakage from adjacent orders. In order not to complicate the scientific analysis of spectra, it is important to keep the AOTF’s sidelobes as small as possible. For NOMAD a sidelobe amplitude suppression of  $-27$  dB is required (4.5% of main lobe), a value that is obtainable by using apodized transducer configurations. Consequently also from an electronics point of view it is important to suppress as much as possible the harmonic frequencies of the applied fundamental radio frequency at the output of the RF driver. For NOMAD the suppression is specified to be better than  $-30$  dB (0.001% of fundamental).

The complete list of specifications for the NOMAD AOTFs is shown in Table 9.

### D. AOTF Optics

The SO and LNO channels have AOTF entrance and exit optics with differently sized clear apertures, curvatures, and focal lengths. The AOTF entrance optics that match the instrument’s entrance aperture (see Table 5) to the acceptance aperture of the AOTF (see Table 9), are telescopes consisting of a Si-Ge doublet lens as objective and a Si singlet as collimator. In SO the magnification of the AOTF entrance telescope is  $5\times$ ,

while in the LNO channel it is only  $1.85\times$ . The AOTF exit optics, which focus the useful beam output by the AOTF onto the spectrometer slit, consist of two ZnSe lenses in the SO channel and of a Ge-Si-doublet in the LNO channel.

### E. Manufacturing and Verification

The NOMAD AOTFs are paratellurite ( $\text{TeO}_2$ ) crystals, custom manufactured under the responsibility of Gooch and Housego, UK. For the delicate operation of mounting the transducers to the AOTF crystals, this company applies specific materials (e.g., the glue to fix the transducer to the crystal) and follows propriety procedures (e.g., thickness of the glue layer). Each crystal-transducer combination gets a hand-tuned matching network aiming to get the input impedance as close as possible to  $50\ \Omega$ . Gooch and Housego own patents on apodization of transducers for sidelobe suppression.

For protection reasons the AOTFs with their matching network are placed in an aluminum box with an entrance and exit aperture. To limit the influence of temperature on the optical properties of the AOTF, it is important that the power dissipated in the crystal is efficiently drained away. For the smaller SO crystal a bottom heat drain is foreseen in AISI 316 stainless steel, a material with a thermal expansion coefficient close to the one of  $\text{TeO}_2$ . For the bigger LNO crystal heat evacuation is foreseen from top and bottom (Fig. 14).

An extensive set of acceptance tests has been performed after delivery of the crystals. One of the most important features to be verified is the sidelobe suppression. This is performed by illuminating the entire aperture of the AOTF homogeneously with HeNe laser light ( $3.39\ \mu\text{m}$ ). The AOTF is mounted on a rotation-and-translation stage that is translated until the laser beam is centered in the entrance aperture and rotated until the diffracted peak falls on a PbSe detector, itself sitting on an independent rotation stage. The AOTF radio frequency is scanned up and down from the central frequency in small steps. Figure 15 gives, both on a linear and a logarithmic scale, the response curve (normalized diffracted intensity versus radio frequency) for the LNO AOTF. It is noted that sidelobes stay nicely below the specified value of 4.5%.

To test the dependence of diffraction efficiency on RF input power, the AOTF is positioned and the RF frequency tuned

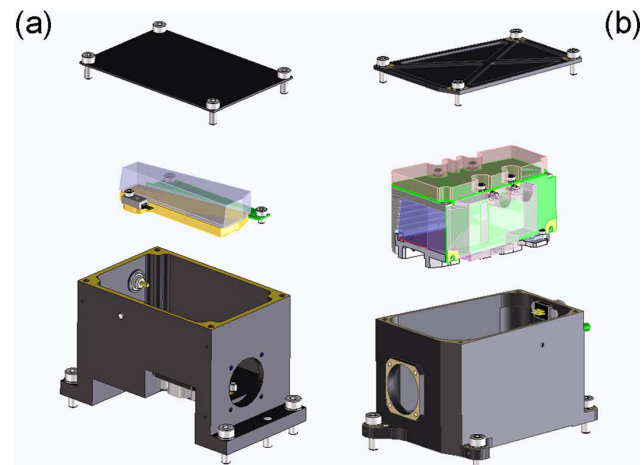


**Fig. 14.** Pictures of NOMAD AOTFs [(a): SO and (b): LNO].

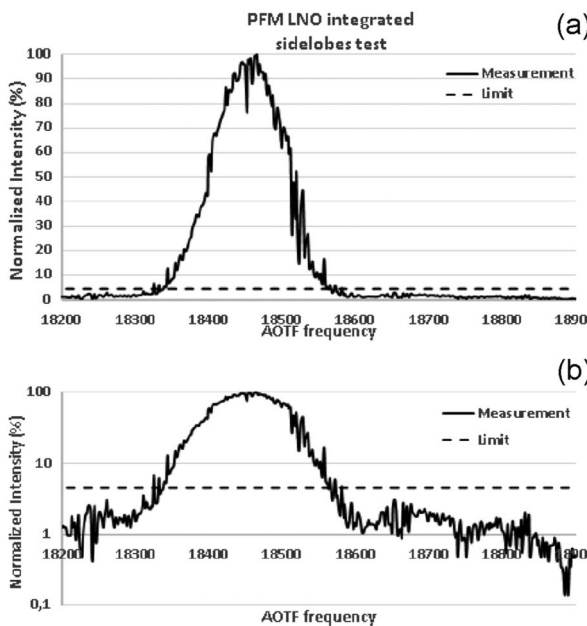


**Fig. 15.** Normalized response curve of the LNO AOTF as a function of radio frequency [(a): linear, (b): logarithmic, dashed line: limit specification of 4.5%].

such that the main diffracted peak falls on the detector. By scanning through the power range from 0 to 2 W (maximum allowable input power) it is seen that for the SO AOTF the specification on the diffraction efficiency ( $\geq 60\%$ ) is met with a value of around 86% for an input power of 1.8 W. For the LNO AOTF the requested diffraction efficiency of  $\geq 80\%$  is met for much higher RF power values (around 8 W). In NOMAD only a maximum of 2 W will be injected into the AOTF, resulting in a suboptimal diffraction efficiency in LNO of about 62% at 2 W. By performing an angular step-scanning of the detector rotation stage with respect to the AOTF, the angle between the undiffracted and diffracted beams is verified. The acceptance angle of the AOTFs is measured by locking the detector again on the diffracted peak, but now performing an angular step-scanning with the AOTF rotation stage (the laser light enters the AOTF under different angles). Figure 16 shows the acceptance angle in the plane of diffraction of the SO AOTF, both on a linear and logarithmic scale. The measured acceptance angle FWHM is  $\pm 2.6^\circ$ , a bit smaller than the required  $\pm 3^\circ$ .

The uniformity of the diffraction efficiency over the entrance aperture of the AOTF is verified by locking the detector and AOTF rotation stages to the diffracted peak, while performing a horizontal and vertical linear step-scanning with the translation stage.

Finally, the voltage standing wave ratio (VSWR) is also registered for each AOTF. While the theoretical input impedance of the AOTF system is expected to be  $50 \Omega$ , in reality it is dependent on the applied frequency. The VSWR gives an indication about the degree of input impedance mismatching. The further the VSWR deviates from 1, the more power will be reflected back from the AOTF. The knowledge of the frequency-to-VSWR relationship of the AOTF is a necessary

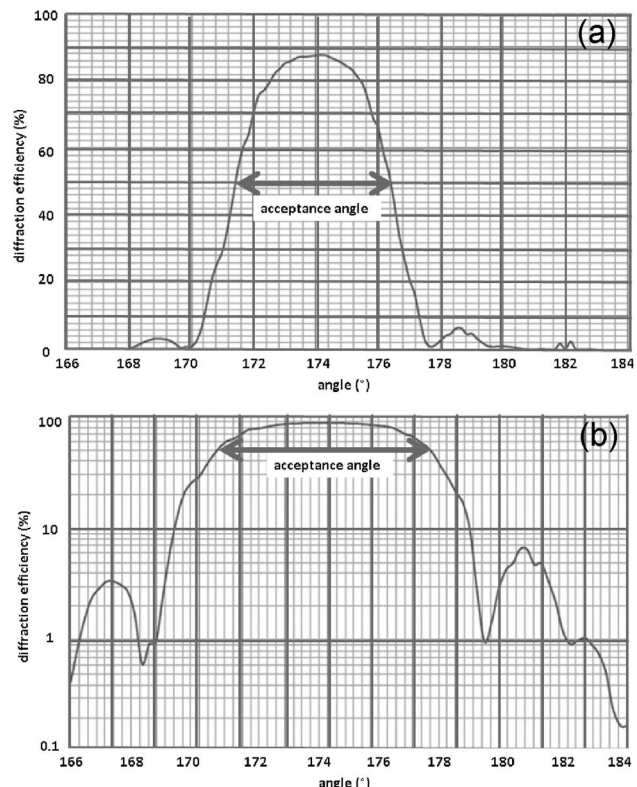


**Fig. 16.** Acceptance angle of the SO AOTF [(a): linear and (b): logarithmic].

input for the design of the electronic RF driver. It should not exceed a value of 3. Figure 17 gives the VSWR curve for the SO AOTF.

## 6. FIELD OF VIEW AND BEAM SHAPING

### A. Spectrometer Slit

The field of view of the SO and LNO channels is fixed by the dimensions of their spectrometer slits. It is explained above how the science requirements led to a slit of  $2' \times 30'$  in SO. Following the Nyquist sampling criterion, it is good design practice to sample the instrumental line profile ( $2'$ ) by at least two detector pixels. The dimensions of the pixels in the selected

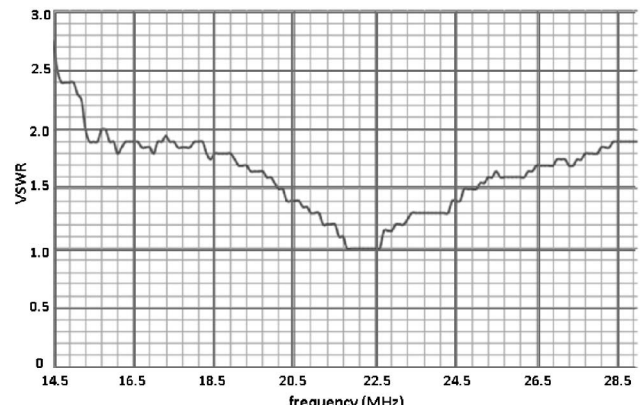


**Fig. 17.** Voltage standing wave ratio (VSWR) of the SO AOTF.

NOMAD detectors (see below) are  $30 \mu\text{m} \times 30 \mu\text{m}$ . Therefore the size of the slit in SO is  $60 \mu\text{m} \times 900 \mu\text{m}$ . To have the same performance in the LNO channel when used in SO mode, at least the part of the slit that is illuminated by the Sun ( $24'$ ) should have been only  $2'$  wide too. To optimize the SNR we have opted for a slit that is  $4'$  wide over its entire length. This results in an SNR that is more than 10% larger compared to the SNR with a slit that has a narrow central part. Increasing also the height of the LNO slit as much as possible in order to increase signal during nadir measurements, its size was fixed to  $4' \times 150'$  or  $120 \mu\text{m} \times 4.5 \text{ mm}$ . To reduce the smile (see also below) of such a high slit on the detector, it is curved (radius of curvature =  $72.5 \text{ mm}$ ) (see Fig. 18). The sag over the central part of the slit that is illuminated by the Sun ( $24'$  or  $720 \mu\text{m}$ ), is less than  $1/30$ th of a pixel and will therefore not be noticed when performing SO measurements.

### B. Diaphragms at the Entrance Pupil

A diaphragm is placed at the location of the entrance pupil, just in front of the first lens of each of the channels. In SO, where the  $f/\#$  of the optics is limited by the entrance pupil, the main purpose of this diaphragm is to better match the footprint of the beam on the grating to the physical size of the grating. This is at the expense of a small loss in light flux of 4%. In LNO the  $f/\#$  is limited by the cold shield. The diaphragm placed at the entrance pupil is slightly larger than the image of the cold shield and serves to minimize the amount of stray light entering the instrument. In Fig. 19 the shape and dimensions of the SO and LNO diaphragm are given. For SO the resulting footprint on the grating, and for LNO the footprints of the beams limited by the cold shield are also shown.

### C. Diaphragms in the AOTF Entrance Optics

The initial purpose of a diaphragm in the entrance optics of the SO AOTF (situated between the objective and the collimator lens sets) was to block superfluous Sun light from entering the instrument. In SOIR at Venus, closer to the Sun, some 70% of the light was blocked. In NOMAD at Mars the image of the Sun on the diaphragm will be approximately half in size, rendering its blocking functionality more or less useless. The diaphragm has not been completely removed, however. It has been enlarged, but such that it still maintains its secondary function, i.e., to prevent that zero-order light from an out-of-field stray light source, entering the AOTF under a critical angle, would

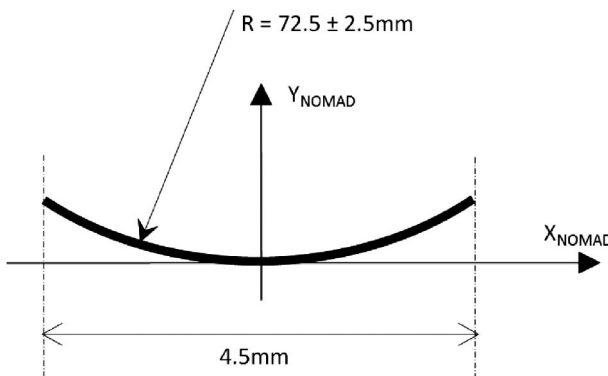


**Fig. 18.** Curvature of LNO slit (exaggerated representation).

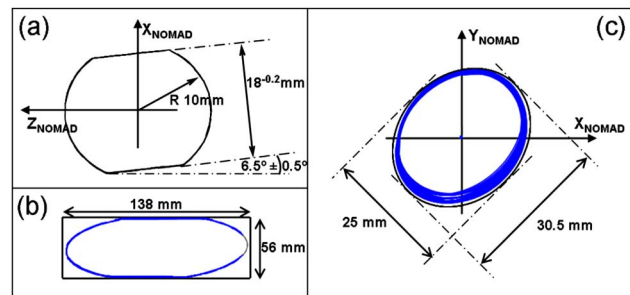


**Fig. 19.** (a) Diaphragm at the entrance pupil for SO and (b) footprint of beam on the grating. (c) Diaphragm at the entrance pupil for LNO and footprints of beam limited by cold shield.

be able to reach the spectrometer slit. In the LNO channel during nadir observations, where the signal will be approximately  $10^6$  times lower than the signal from the Sun, it is even more vital that zero-order light cannot pass the AOTF and reach the spectrometer slit and hence to use a narrow enough diaphragm.

## 7. DETECTORS AND READOUT ELECTRONICS

### A. Detectors and Coolers

As described above, the parabolic mirror forms an image of the spectrometer slit and projects it on the detector's sensitive area with a magnification of 1. The position of the detector is inclined so that its optical axis coincides with the optical axis of the imager optics and to bring its pixel columns in line with the image of the spectral lines produced by the grating.

The detector used in NOMAD is the standard MARS-MW K508HSM integrated detector Dewar cooler assembly manufactured by Sofradir, France. This MARS-MW detector is a photovoltaic mercury cadmium telluride (MCT) detector with a focal plane array (FPA) of 320 columns by 256 rows and  $30 \mu\text{m} \times 30 \mu\text{m}$  sized pixels. The FPA is lodged in a vacuum Dewar with a customized 1 mm thick silica front window (refractive index  $n = 3.4$ ) with antireflective coating. In the Dewar a cold radiation shield with an  $f/3.936$  aperture shields the FPA thermally from its surroundings. The aperture of the cold shield is precisely aligned with the detector pixels. The FPA is cooled down by a K508HSM rotative Stirling cooler (manufactured by Ricor, Israel). The off the shelf version of this detector is modified for the NOMAD application. It has a different cooler body and the integrated cooler motor control circuit has been discarded and replaced by an external space qualified design of BIRA-IASB. But the most important adaptation is the customization of the wavelength range. The material of the Dewar window (Si) defines the cut-on wavelength (around  $2 \mu\text{m}$  at 50% of maximum response). The MCT composition of the FPA defines the cutoff wavelength. This is true for the SO detector (around  $4.2 \mu\text{m}$  at 50% of maximum response). In LNO, however, a 0.3 mm thick germanium cold filter (refractive index  $n = 4$ ) is added on top of the cold shield, cutting short the wavelength range (cutoff wavelength around  $3.9 \mu\text{m}$  at 50% of maximum response). In Fig. 20 the normalized spectral responses of the SO and LNO detectors are shown.

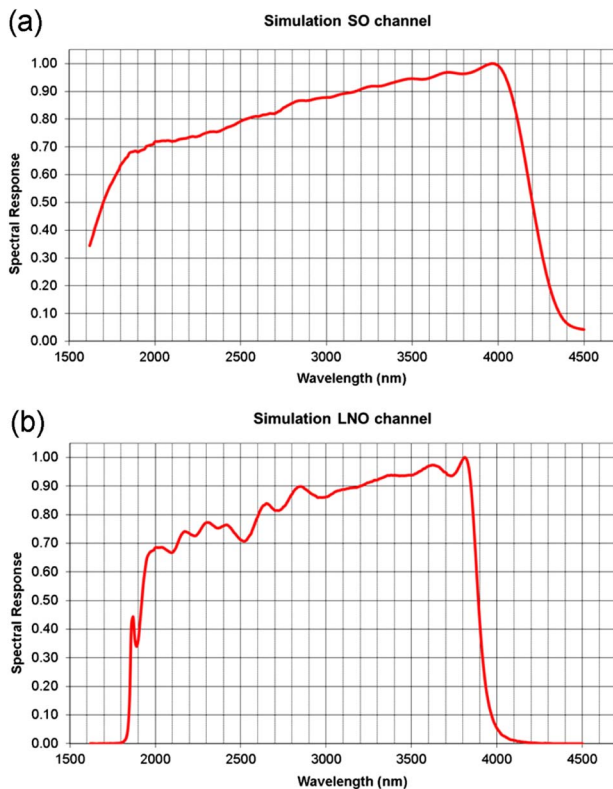


**Fig. 20.** Normalized spectral response of detectors: (a) SO and (b) LNO.

In SOIR on Venus Express a K508 cooler from Ricor was used. This cooler has a declared lifetime (MTTF) of  $\geq 8000$  h, which is sufficient for SO missions (SOIR, NOMAD SO channel) but not for nadir missions (NOMAD LNO channel). A solution offering a significant increase in MTTF was proposed for NOMAD with Ricor's K508HSM, a derived product from K508 with modified stator coil windings allowing a lower operating pressure and, hence, reduced pressure on the compressor's ball bearings. The expected MTTF for the H508HSM is  $\geq 12,000$  h.

This detector-cooler assembly is extensively described in the literature [13]. An overview of the rest of its characteristics is given in Table 10.

### B. Readout Electronics

When an IR photon with wavelength below the cutoff impinges on the MCT sensitive area, it creates an electron-hole pair that is immediately separated by the internal electrical field of a photovoltaic diode. The  $320 \times 256$  photovoltaic diodes (pixels) are individually coupled by indium bump technology to a raster of charge capacitors laid out on a CMOS readout integrated circuit (ROIC) at the back of the FPA. For the duration of the programmed integration time, the capacitors are fed with the electrons from the photovoltaic diodes by direct injection and store the charge. At the end of the integration process all the charges are converted to voltages and multiplexed into an analog video signal at the output of the ROIC. A consequence of using the direct injection method is that the linearity of the readout is not guaranteed for low signals and for

**Table 10. Detector and Cooler Characteristics for the SO and LNO Channel**

Parameter	SO	LNO	Unit
Number of pixels per column	256		
Number of pixels per row	320		
Pixel size	$30 \times 30$		$\mu\text{m}^2$
Cold shield aperture ( $f/\#$ )	$f/3.936$		
Integration capacitor (gain 0/gain 1)	0.7/2.1		pF
Maximum charge (gain 0/gain 1)	12.0/37.0		$10^6 e^-$
Video output range	1.6–4.4		V
Video dynamic range	2.8		V
Minimum integration time	3		$\mu\text{s}$
Wavelength range (50% of response)	2.0–4.2	2.0–3.9	$\mu\text{m}$
Typical quantum efficiency at $3.5 \mu\text{m}$	0.75		$e^-/\text{photon}$
Linearity (charge 7% to 97% of pixel saturation)	95		%
Readout speed for single video output	1		MHz
Typical focal plane temperature	90		K
Cool down power consumption (273 to 90 K)	10.6		W
Regulated temperature power consumption (at 90 K)	3.8	3.5	W
Cool-down time (273 to 90 K)	261	266	s

signals close to saturation (see Table 10). It is important to note that this type of detector has a windowing mode, allowing to readout only a reduced window of detector pixels.

Using the FPA at temperatures above 130 K could harm the detector. Therefore, two diodes are integrated in the FPA and used as temperature sensors (injecting a constant current, then measuring the voltage over the diode that is proportional to the temperature). They allow the control loop to verify if the requested cold FPA temperature setting (typically around 90 K) is reached.

## 8. SYSTEM CONTROL ELECTRONICS, FIRMWARE, AND SOFTWARE

### A. Channel Electronics

Both the SO and the LNO channels have a completely separate dedicated space qualified electronic control unit (Fig. 21). In this unit one can distinguish three chains, one for each of the three electronically driven devices: the AOTF, the FPA, and the cooler. The three chains are controlled from a central control and communication board (CCC) that is built around a Xilinx field programmable gate array (FPGA). For the AOTF chain, a direct digital synthesizer is implemented inside the FPGA that produces a code that represents digitally the radio frequency sine waveform that has to be applied to the AOTF. This code is transformed in an analog signal on the radio frequency generator board (RFG). This low-power RFG signal is then amplified in a radio frequency power amplifier, the design and manufacture of which has been subcontracted to a specialized company (ERZIA, Spain). Finally, the amplified RF signal is applied to the AOTF's matching network and transducer.

The design of the radio frequency power amplifier focused on spectral quality. Since the power amplifier frequency range

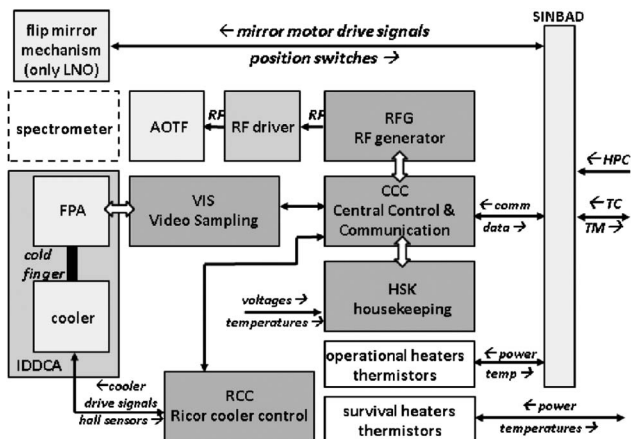


**Fig. 21.** Block diagram of electronics of SO and LNO channel.

covers approximately one octave, it is important that the second harmonic of the generated carrier is suppressed as much as possible ( $\leq -30$  dBc). A customized amplifier design was implemented and an extra sharp low-pass output filter added to remove any remaining unwanted spectral components. Low DC power consumption ( $\leq 6$  W) was set out as a critical requirement because of the limited DC power resources in NOMAD. In the power amplifier design physical properties were taken into account, such as input impedance, voltage standing wave ratio (Fig. 17) and RF input power, all as a function of wavelength, of the real AOTFs. Also the diffraction efficiency of the AOTFs as a function of AOTF input power was a driver during design. Table 11 gives an overview of the characteristics of the power amplifier. Figure 22 shows the second and third harmonics levels for the SO channel power amplifier. It is clearly seen that the initial requirement of harmonic suppression under  $-30$  dBc could not be met. Figure 23 shows that the DC power of the amplifier is successfully kept below the specified value over the complete wavelength range and for different amplifier RF output power levels.

A second chain in the channel electronics concerns the detector. The FPGA on the CCC board generates the clock

**Table 11. Characteristics of the SO RF Power Amplifier**

Characteristic	Value or Range	Unit
RF frequency band	14.2–28	MHz
Maximum RF input power (at 14 MHz)	2.16	dBm
Maximum RF input power (at 28 MHz)	0.73	dBm
Input impedance	50	$\Omega$
Maximum RF output power	33	dBm
	2	W
RF output settling time	<1	ms
Unwanted spectral components, e.g., harmonics	< -30	dBc
Efficiency at maximum RF output	33	%
Nominal load (AOTF impedance)	50	$\Omega$
Acceptable AOTF VSWR	1–3	
Supply voltage	11.82–12.18	V
Maximum allowed DC power consumption	6	W

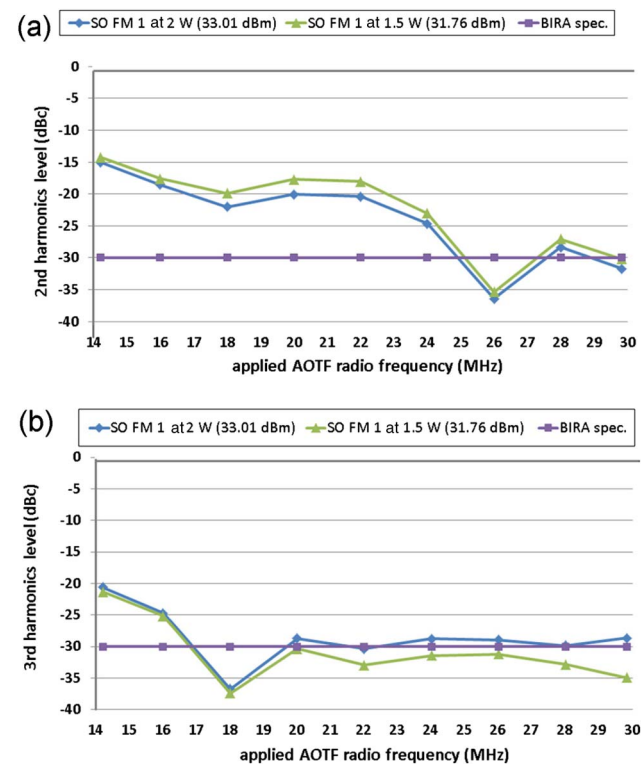


**Fig. 22.** (a) Second and (b) third harmonics levels of the radio frequency power amplifier (SO).

signals and other parameter settings (gain, window mode) needed to read out the FPA. The analog video signal from the detector (see above) is sampled on the VIS board, amplified, converted to digital, and transferred to the CCC board.

The third chain is used to drive the cooler. The FPGA sends a digital control signal, representative for the desired motor speed, to a digital-to-analog convertor on the RCC board. The resulting analog signal is used as input to a motor controller hybrid that generates pulse-width-modulated phase signals to drive the brushless three-phase DC motor of the cooler. Three hall sensors detect the position of the motor rotor and are fed back to the motor controller.

Besides the three main chains, the channel electronics also contains a housekeeping board that collects measurements

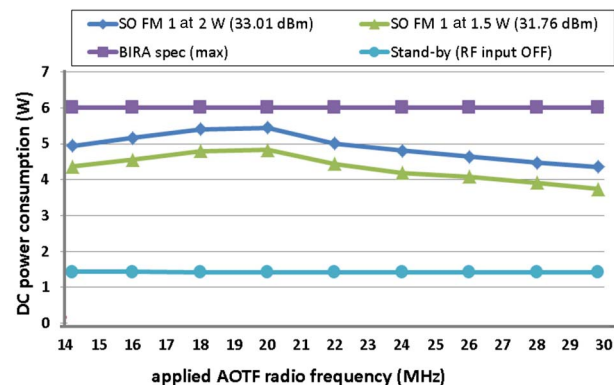


**Fig. 23.** DC power of the radio frequency power amplifier (SO).

from temperature, voltage and current sensors, digitalizes them and returns them over multiplexers to the FPGA on the CCC board.

### B. Front Line Power and Control Unit (SINBAD)

The electrical interface between the NOMAD instrument and the spacecraft is not situated in the channels themselves. The SO, LNO, and UVIS electronics interface to NOMAD's front line power and control unit (SINBAD). SINBAD can be switched on and off by the spacecraft through high power commands. While on, it is powered by an unregulated voltage and can interact with the spacecraft through a MIL-standard 1553 bus (uploading telecommands, downloading housekeeping data) and a SpaceWire link (downloading science data). SINBAD switches on and off each of the three NOMAD channels depending on the imposed observation timeline (see below). It regulates the primary power and offers a stable voltage to the channels. SINBAD is built around two Actel FPGAs. The primary FPGA (Shireen) contains a firmware LEON3 microprocessor running a real-time operating system (RTEMS) to which a series of software management functions are added, among which are a telecommand interpreter and a file operation management system allowing versatile use of the available on-board memory. The secondary FPGA (Chimera) controls the flip mirror mechanism (only in LNO) and NOMAD's operational heaters and thermistors (see below), but has to be seen primarily as a firmware extension of the SO and LNO channels. Chimera streamlines the registration of spectra in these channels by sending them in a timely manner command packets and by capturing in memory, at high speed, the data stream they send back on the fly.

During ground testing, the instrument can be operated from a dedicated electrical ground support equipment, running a user-friendly software interface developed in Python.

Electrical components in NOMAD are selected to be radiation tolerant, compliant to the total dose requirement of the TGO mission, and immune against latch-up and single event effects. During mechanical design sufficient aluminum shielding has been foreseen. It is confirmed by sector analysis that NOMAD is radiation protected throughout the mission.

## 9. OBSERVATION SEQUENCES AND MODES

The science operations during one orbit around Mars can be split in four distinct observations. At dayside NOMAD will perform nadir observations with the LNO and UVIS channels. At the sunset terminator a SO measurement will be performed with the SO and UVIS channels. At nightside atmospheric emission measurements can be done with LNO and UVIS. At the sunrise terminator a SO measurement will be performed with SO and UVIS. Thanks to the presence of the flip mirror in LNO, it is also possible to use LNO instead of SO during SOs. Using SO and LNO at the same time is excluded due to spacecraft power limitations.

Just before starting a nadir observation or SO measurement with one of the infrared channels it is necessary to cool the detector down to its operating temperature of approximately 90 K. A command packet is sent to the channel to start this precooling phase. This packet contains parameters such as

the cooler temperature set point, an open or closed loop flag, and some cooler coefficients allowing smooth regulation. During precooling (duration is maximum 600 s, depending on the temperature of the environment) no spectra are recorded, only housekeeping is sent every second. At the end of the pre-cooling phase, the channel starts a science observation upon reception of a new command packet. This time the command contains parameters that will permit the channel to do "real" measurements, such as the AOTF frequency and AOTF power set points, the detector integration time, window frame dimensions, the binning factor, and more. For nadir, longer integration times are anticipated and therefore the typical sampling time is 15 s. During SOs integration times will be much shorter and the sampling time is 1 s.

The on-board software of the channels offers a wide range of features to tailor the measurements to the scientific needs. During one measurement, i.e., in the time frame of 1 s (SO) or 15 s (nadir), it is possible to perform up to six consecutive measurements, each with different parameter settings. In this so-called hopping mode it is, e.g., possible to measure in six randomly chosen spectral domains (six AOTF frequency settings corresponding to six grating orders). It could be an option to dedicate one of the "domains" to a dark measurement with the AOTF switched off. Moreover, it is possible to switch from a set of six initial subdomains (used during the first half of the observation) to six totally different subdomains in the second half. This is especially useful during SO where the science interest in the upper atmosphere can be quite different from that in the lower atmosphere.

Accumulation is a technique that, inside one subdomain measurement, allows increasing the SNR of the measurement by adding a series of consecutively registered spectra. The recording of a spectrum, i.e., the frame that is read-out from the detector after one integration time slice, could be repeated a number of times and added in memory to the accumulated pixel-by-pixel sum of the previous ones. While the subdomains have to fit within the time frame of one measurement (1 and 15 s for SO and LNO, respectively), the combination of integration time and number of accumulations has to fit within the duration of one subdomain measurement. Figure 24 shows an example of a NOMAD observation sequence for one orbit.

When composing commands for the SO and LNO channels it is important that the time combination of integration times, processing times, number of accumulations, and number of subdomains stays within the sampling time. Besides a hopping mode, NOMAD can be commanded in stepping mode, meaning that from one measurement to the next, a parameter (e.g., frequency, integration time, window top, etc.) is incremented by a step value. The stepping mode can be handy during on-ground or in-flight calibration of the channels, when, e.g., the full detector window has to be read or a frequency scan over the whole spectral domain has to be performed. NOMAD calibration will be reported upon in a separate publication [14].

For each recorded spectrum, all illuminated detector lines are read-out by the channel electronics, i.e., 24 lines in the SO channel and the LNO channel when working in SO mode, and 144 lines in the LNO channel when working in nadir mode. However, due to data rate limitations at spacecraft side, during

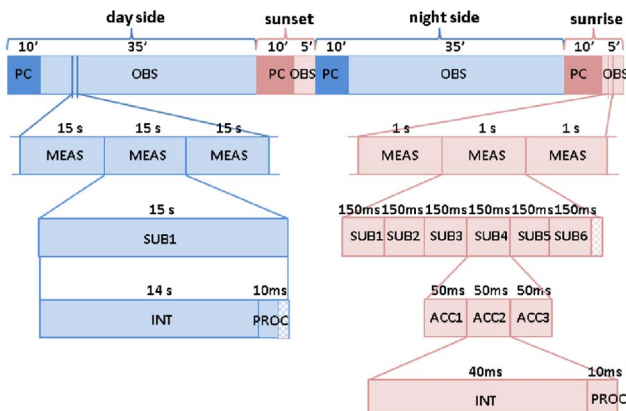


**Fig. 24.** NOMAD observation sequence. PC, precooling; OBS, observation (nadir or SO); MEAS, measurement; SUB, subdomain; ACC, accumulation; INT, integration time; PROC, process time (including detector read-out, AOTF settling, etc.). Left (blue): nadir observation with one subdomain, no accumulation, spectra with 14 s integration time. Right (red): SO observation with six subdomains, three accumulations in subdomain 4, spectra with 40 ms integration time.

one sampling time only the equivalent of 24 detector lines can be processed by the spacecraft and transmitted to Earth. This has a number of consequences on NOMAD's observation philosophy. First of all, this means that in LNO the 144 read lines will be always reduced to 24 "superlines" through binning by six. If a measurement consists of only one subdomain the 24 read (super)lines will all be transmitted to Earth. If a higher number of subdomains is used per measurement, a corresponding line binning will be applied. For the example at the right side of Fig. 24, where a measurement consists of six subdomains, binning by six will be applied to the lines, and only four "superlines" will be processed per subdomain. Binning of lines has an impact on the spatial resolution of the channel.

The severe limitation in allowable number of payload telecommands during this ExoMars mission ( $\leq 10$  telecommands per orbit for NOMAD) has resulted in the implementation of on-board channel observation parameter tables with a nearly unlimited number of preprogrammed combinations of instrumental parameters. If modifications still appear to be necessary, these tables can be patched from ground.

## 10. MECHANICAL STRUCTURE, STRUCTURAL ANALYSIS, AND ALIGNMENT

### A. Mechanical Structure

NOMAD is housed in an aluminum structure, consisting of two base plates, the bottom one serving as an optical bench for the SO channel, the top one for the LNO channel. A set of carrier walls interconnects the SO and LNO base plates. The base plates are flat topped but have a ribbed structure at the bottom in order to reduce weight but maintain strength and stiffness. The useful surfaces are  $428 \times 306 \text{ mm}^2$  for the SO optical bench and  $439 \times 316 \text{ mm}^2$  for the LNO bench. On the SO base plate an area is kept free where the UVIS channel, which sits on its own intermediate base plate, is located. The

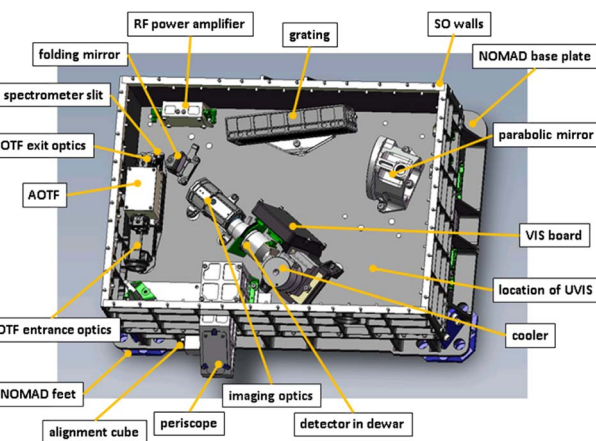


**Fig. 25.** 3D view of the SO channel.

thickness of the SO plate is 90 mm and is 56.8 mm for the LNO plate. The SO base plate is thicker because it has a box shape, open at the bottom, that is used to lodge SINBAD and the electronic units of the SO and LNO channels. Figures 25 and 26 show 3D drawings of the SO and LNO base plates. The important mechanical elements can be recognized in each channel: a SO periscope carrying the entrance mirrors, an AOTF bridge carrying the AOTF box and the AOTF entrance and exit optics, the support of the grating (milled from one block together with the optical part), the support of the parabolic mirror (milled from one block together with the optical part), some optical mounts (for spectrometer slit, folding mirror, imaging optics), and the foot for the detector-cooler assembly. Only two electronic modules, each in their mechanical box, are present on the optical bench: the VIS board (close to the detector) and the RF power amplifier (close to the AOTF). The walls of LNO and the top cover do not serve any structural goal. Together with the SO walls, they are merely used as support structure for the MLI that encloses the whole of NOMAD (see below). The complete +Z-side wall of NOMAD and a small part of the top cover (+X-side) are manufactured in

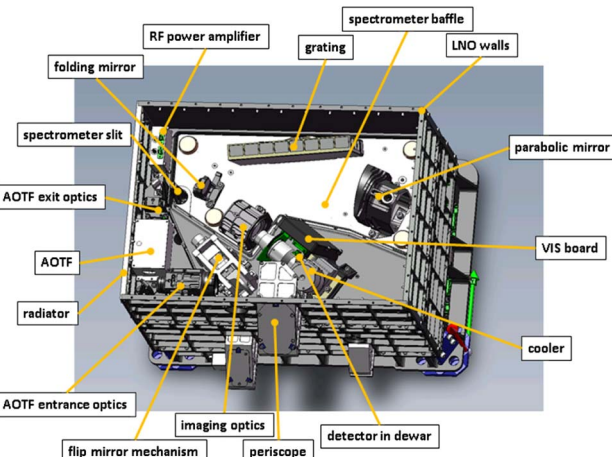


**Fig. 26.** 3D view of the LNO channel.

one piece and serve as radiator (see below), as it is directed toward deep space in most phases of the mission.

In the electronic section, at the bottom of the SO base plate, all the electronic boards are protected by individual mechanical boxes. From this section the harness, which is manufactured by Glenair, UK, is routed up to the three channels.

Nearly all mechanical parts are made in 7075-T7351 thermally pretreated aluminum. For better manufacturability some optical parts are made from 6061-T6 aluminum (gratings, flip mirror) or RSA-6061 aluminum (parabolic mirrors). Most of the mechanical elements, and especially those close to the optical path, have undergone a space qualified optically black anodization (Protection des Métaux, France). This should limit scattering of light and keep the influence of thermal background as low as possible. Contact surfaces between mechanical parts are kept free of anodization but have been treated with alodine 1200 for good electrical conductivity. In order to achieve good thermal contact between base plates, walls and optical mounts, mechanical provisions are foreseen in the contact planes where thermal filler can be placed. The outside of the radiator part has been painted white (see below).

The most noticeable exceptions to the all-aluminum approach are the three NOMAD feet that form the mechanical interface to the spacecraft. In order to insure the thermomechanical stability of the spacecraft instrument deck, a very low thermal conductance is imposed between the instrument and the spacecraft. Therefore, the feet are made from titanium, which has a 10 times lower thermal conductivity than aluminum, and contain a double intrinsic thermal barrier, one in the mounting plane to the spacecraft ( $3 \times M8$  screws) and one at the interface of the feet with the instrument ( $4 \times M5$  screws). Despite the dedicated mechanical design a noncompliance is reported on the thermal conductance between NOMAD and the spacecraft (see below). The three feet have crumple zones giving them sufficient elasticity to act together as isostatic mount for the instrument, limiting the transfer of elastic deformation from the spacecraft deck to the instrument and vice versa.

## B. Structural Analysis

A very detailed structural analysis was performed using a finite elements mathematical model (MSC NASTRAN 2010) based on the CAD model of the instrument. The stiffness has been verified by normal mode analysis. Eigenfrequencies are calculated for the 3 translational and the 3 rotational degrees of freedom, each with its associated modal effective mass (MEM). In Fig. 27 it can be seen that the requirement of a first overall eigenfrequency of the instrument  $\geq 140$  Hz is not met.

Two modes (117.8 Hz and 131.9 Hz) are found below this limit with nonnegligible MEM. Further, a quasi-static load analysis was performed on the interface bolts for load cases along different directions. The results show no surpassing of the maximum allowable load on the deck inserts (2046 N axial, 1665 N in mounting plane). Also a stress analysis was done on the titanium interface feet showing that, although stress is highest in the regions of the bolt holes and the elasticity "hinges," the modeled values are below the stress limit values for titanium. Finally, in preparation of later vibration tests on the "real" instrument, loads have been simulated for sine and random vibrations.

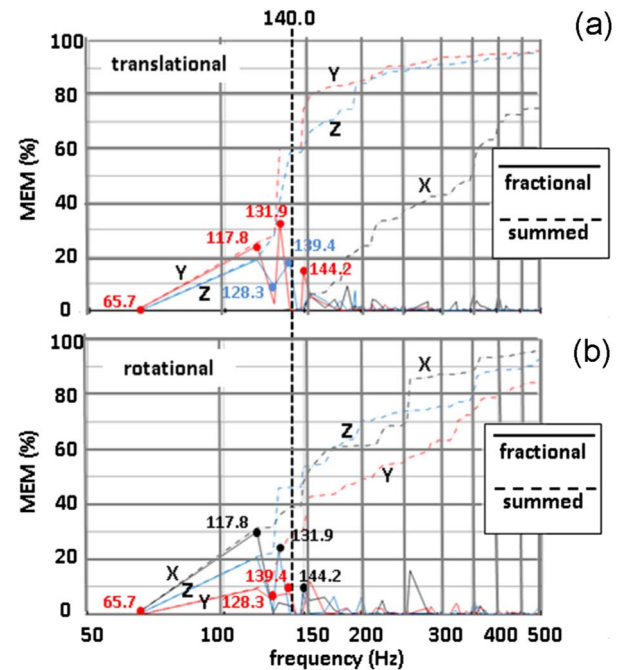


**Fig. 27.** Normal mode analysis result: modal effective mass (MEM) as a function of frequency. Six first eigenfrequencies are indicated with dots. Continuous line is fractional MEM, dotted line is summed MEM. (a) translational degrees of freedom; (b) rotational degrees of freedom.

Qualification level vibration and shock tests were run successfully (CSL, Belgium and IABG, Germany) on the so-called structural thermal model (STM) of the instrument, a model that is completely representative for the flight model as to what mass, center of gravity, and moments of inertia are concerned. The test results obtained on the STM have been correlated with the mathematical model predictions. The tests were repeated with acceptance level loads on the proto flight model (PFM).

## C. Flip Mirror Mechanism

A movable mirror, the so-called flip mirror, selects, as input for the LNO channel, either the light beam from the nadir or from the solar entrance. The nadir and solar positions of the mirror correspond to the two end positions of the mechanism carrying the mirror. The nominal position of the flip mirror is "nadir." During launch the flip mirror will be placed in an intermediate position offering the best resistance to vibrations. While in the "solar" position the only constraint is that the mirror is completely out of the beam, in "nadir" some in-beam position accuracy is required ( $\pm 5$  mrad). The mirror is mechanically aligned such that it makes an angle of exactly  $45^\circ$  with the optical axis, fulfilling the accuracy requirement. The movement of the mirror in the reflection plane, however, does not guarantee this accuracy, reason why its surface is slightly oversized. A stepper motor-demultiplicator system (Thales Alenia Space, France), which is suspended in an aluminum cradle-in-craddle structure, drives the mirror through a worm-worm wheel gear. In normal operation the cradles are kept solidary by means of a pin, but in the case of a motor failure, the pin can be retracted (pin puller), so that a spring-assisted separation of the cradles

will take place and the mirror will be forced definitely in its fail-safe position (= “nadir” position). In the two end positions a nominal and redundant position switch are mounted and a hard stop as well. Figure 28 is a 3D drawing of the flip mirror mechanism.

#### D. Optical Coalignment

The NOMAD instrument has three periscopes protruding from the -Y-face of its main volume, one in each of the channels, allowing them to perform SO measurements at the Martian limb ( $67.07^\circ$  off the nadir direction). While the optical coalignment of the nadir lines of sight is driven solely by the mechanical tolerances on the parts, the periscopes are designed to have accessible and adjustable primary mirrors in each of them, allowing coalignment of the three solar lines of sight (see Fig. 2). In fact, all lines of sight are aligned with respect to NOMAD’s main alignment cube, sitting on the -Y-face of the SO base plate (see Fig. 25). This cube will also be used during integration on the spacecraft for checking the misalignment with the spacecraft’s mechanical axes. This misalignment is important during flight when the pointing direction of the spacecraft has to be calculated.

## 11. THERMAL ENVIRONMENT

### A. Geometrical and Thermal Model

An instrument on an interplanetary mission, and especially on ExoMars where the payloads are exposed to open space, can be subject to extreme thermal environmental conditions. The following cases have been studied: a cold survival case during cruise phase, a cold nonoperational case during the long eclipse right after Mars orbit insertion, a hot aerobraking case, and the standard hot and cold operational cases during science phase. For all of these cases temperature predictions have been made in a CAD-model-based thermal and geometrical mathematical model (ESATAN TMS). In this model all external and internal elements impacting the thermal behavior of NOMAD have been taken into account.

External factors are the radiative and conductive coupling with the spacecraft, the neighboring instruments, and the space environment (deep space, Mars, Sun at different  $\beta$ -angles, aerobraking flux) at NOMAD’s thermal interfaces, i.e., the three low conductance feet, the MLI, the radiator, and the optical apertures.

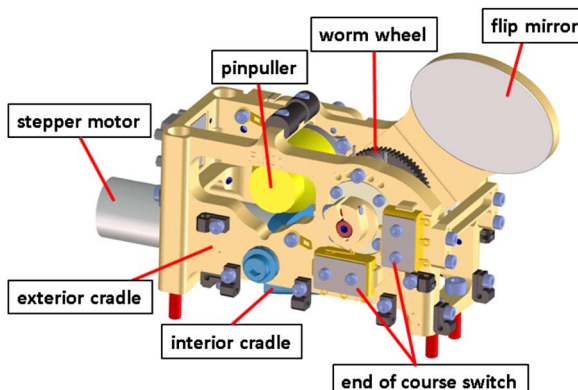


**Fig. 28.** Flip mirror mechanism.

The three interface feet of NOMAD have to fulfill a very stringent thermal conductance requirement ( $\leq 0.02 \text{ W/K}$ ). Thermal conductance tests were performed (Mechanical Systems Laboratory, Thermal Division, ESTEC, The Netherlands) on a sample foot showing values between  $0.022 \text{ W/K}$  at  $-43^\circ\text{C}$  and  $0.036 \text{ W/K}$  at  $26^\circ\text{C}$  per foot (uncertainty margin 8%). This noncompliance with the requirement has been assessed and accepted by ESA. Except for the radiator and the entrance apertures, NOMAD is completely wrapped in MLI with a 12-layer lay-up including XC100/VDA kapton black layers at inside and outside (solar absorptivity  $\alpha_{\text{MLI}} = 0.93$ , infrared emissivity  $\epsilon_{\text{MLI}} = 0.84$ ) (manufactured by HPS, Germany, and HPS, Portugal). The thermal blanket consists of nine individual pieces matching together and to the spacecraft MLI. The MLI is designed for continuous working at temperatures between  $-200^\circ\text{C}$  and  $+150^\circ\text{C}$ , and for surviving instant peak temperatures up to  $+392^\circ\text{C}$ . The radiator is covered by a  $120 \mu\text{m}$  layer of SG121FD silicone paint (MAP, France) for optimal heat rejection (solar absorptivity  $\alpha_{\text{rad}} = 0.27 \pm 0.02$ , infrared emissivity  $\epsilon_{\text{rad}} = 0.88 \pm 0.03$  at  $+20^\circ\text{C}$  and  $0.77 \pm 0.03$  at  $-182^\circ\text{C}$ ). The sizing of the radiator’s surface area ( $9.011 \text{ dm}^2$ ) was driven by the need to cool down the instrument as much as possible (reduction of thermal background, especially in LNO) at one side, and by the restriction to not pass the lowest acceptable non-operational temperature for sensitive elements as, e.g., the two AOTFs.

Internal thermal factors are the material and surface properties, the conductive boundary conditions between parts (0.38 mm thick Chotherm-1671 is used as thermal filler), the internal power dissipation during nominal operation (38.1 W average and 47.9 W peak, independent of voltage), and power dissipation distribution during operational hot cases, the operational heaters (14.4 W, controlled by SINBAD during operational mission phases) and the survival heaters (16 W at 22 V, controlled by independent thermostats with switch-on at  $-15^\circ\text{C}$  and switch-off at  $-10^\circ\text{C}$  during survival phases).

The model shows that for the coldest case (long eclipse) the survival heater power of 16 W keeps all temperatures within limits, provided that the heater power distribution is adapted to the temperature gradient inside the instrument (more power near coldest parts). From the model it is seen that in the cold operational case, all temperatures are within limits and hence the operational heater powers are superfluous, unless one of the channels would remain switched off. In the hot operational case the temperatures in the electronics boxes tend to exceed their limit value of  $+50^\circ\text{C}$ . If this worst case situation would appear during flight, an ultimate mitigation could be to keep the internal power dissipation lower by letting the channels work alternatively.

From the model it follows that, for typical thermal cases, both optical benches will be kept at a temperature between  $-10^\circ\text{C}$  and  $+10^\circ\text{C}$ . During SOs (measuring time typically 5 min) the fluctuation of the bench temperature due to internal heating is negligible. During longer nadir observations (typically 40 min) bench temperature can increase by  $2^\circ\text{C}$  to  $5^\circ\text{C}$ , decreasing slightly the SNR response of the instrument.

A sensitivity analysis has been performed looking at potential impact of variation in thermal parameters ( $\alpha_{\text{rad}}$ ,  $\epsilon_{\text{rad}}$  and

area of the radiator, thermal capacity and conductivity, power dissipation, contact resistance, MLI conductance) between the uncertainty boundaries. None of the parameter variations leads to worrying increase or decrease in the model temperatures.

### B. Thermal Tests

Qualification level thermal balance and thermal cycling tests in a vacuum environment have been performed on the STM (CSL, Belgium). The STM is fully representative for the thermal behavior of the flight model (identical radiator and MLI, operational and survival heater chains present plus a separate heater chain to simulate the internal power dissipation). The test results obtained with the STM have been correlated with the mathematical model predictions. The thermal tests are repeated at acceptance level on the PFM.

From an optical point of view, the ideal working temperature is between  $-5^{\circ}\text{C}$  and  $+5^{\circ}\text{C}$  because optics are optimized for this temperature range. For SNR reasons the lower the temperature, the better.

## 12. THERMAL BACKGROUND, SIGNAL, AND NOISE

The SNR defines the sensitivity of an instrument. Especially in the LNO channel during nadir observations, where the expected incoming signal is  $10^6$  times weaker than in LNO or SO during SO measurements, suppression of the system noise is important. One of the most important sources of noise is the thermal background, which is highly temperature dependent. The higher the temperature of the instrument, the higher the thermal background. A broad range of parameters have an influence on the SNR, acting either on the portion of incoming signal that reaches the detector ( $S$ ), the thermal background (TB), or on the noise ( $N$ ). The  $F$ -number of the optics defines the amount of light collected and hence the signal intensity. A good matching between the  $F$ -numbers of the optics and the detector is advantageous for the SNR. In SO there is a mismatch ( $f/5.12$  for the optics,  $f/3.936$  for the detector) resulting in the detector seeing also part of the walls. In LNO this has been prevented by equalizing the  $F$ -number to  $f/3.936$  over the whole chain. An additional advantage is that in LNO the height of the slit could be increased to cover the full etendue of the system ( $150'$  in LNO against  $30'$  in SO). At the same time the slit in LNO has been made wider ( $4'$  in LNO against  $2'$  in SO). The signal will be influenced also by the bandwidth and the diffraction efficiency of the AOTF. For LNO the bandwidth is slightly larger than for SO ( $24\text{ cm}^{-1}$  against  $22\text{ cm}^{-1}$ ) while the attainable diffraction efficiency with an RF power up to  $2\text{ W}$  is somewhat lower (62% in LNO against 86% in SO). Likewise the transmission of the grating impacts the signal. The diffraction efficiency of the grating varies over wavelength and hence is different from order to order and, due to the dispersion inside one order, also from pixel to pixel. The SNR can be up to 4 times lower at the edges of the free spectral range (or the detector array) compared to the central pixel. Another important element is the cutoff wavelength of the detector. In LNO this cutoff is different from the one in SO ( $3.9\text{ }\mu\text{m}$  against  $4.2\text{ }\mu\text{m}$ ) due to the presence of a cold filter. Finally, the SNR can be significantly improved by reducing the thermal background,

i.e., by cooling the optical and mechanical elements that are within the field of view of the detector.

The LNO channel was initially designed to have a cooled spectrometer section ( $-100^{\circ}\text{C}$ ), but the design was abandoned in a late stage, due to weight limitation issues. One additional obstacle was the fact that, even with a cooled spectrometer in front of the detector, the detector window itself remained still at high temperature, and would undo largely the gain obtained by the cooling. This means that the initial goals of an overall SNR during LNO nadir observations of  $\geq 400$  and a maximum of  $\geq 1000$  in the methane band cannot be met.

For the calculation of the incoming signal during SOs the spectral radiance of the Sun  $L_{\lambda s}$  is used, which is independent of the position of Mars [15]. For nadir observations, however, the spectral irradiance of the Sun at Mars  $E_{\lambda m}$  is used,

$$E_{\lambda m} = \frac{\pi \cdot R_S^2}{D^2} \cdot L_{\lambda s}, \quad (12)$$

with  $R_S$  the radius of the Sun and  $D$  the distance Mars–Sun. Hence, this spectral irradiance depends on the position of Mars with respect to the Sun. From  $E_{\lambda m}$  the spectral radiance  $L_{\lambda m}$ , emitted by the Martian disk, can be derived,

$$L_{\lambda m} = \frac{A}{\pi} \cdot E_{\lambda m}, \quad (13)$$

where  $A$  is the albedo of Mars. The signal level on the detector is calculated by applying the channel's transmission function to the incoming signal. The instrument transmission function is derived for each pixel across the detector array and each grating diffraction order as the product of the above-described optical parameters of optics, grating, and AOTF. For SO the signal on the detector can be expressed as

$$S_{\lambda} = \frac{a \cdot \pi}{4 \cdot F^2} \cdot \Delta\omega \cdot W_{\text{slit}} \cdot T_{\text{opt}}(\lambda) \cdot L, \quad (14)$$

with  $F$  the channel's  $F$ -number,  $a$  the pixel area,  $\Delta\omega$  the pixel bandwidth (or spectral sampling interval, SSI),  $W_{\text{slit}}$  the slit width,  $T_{\text{opt}}(\lambda)$  the transmission of the optics, and  $L$  the radiance ( $L = L_{\lambda s}$  for SO and  $L = L_{\lambda m}$  for LNO). The signal  $S$  received on a detector pixel in  $\text{e}^-/\text{s}$  is given by

$$S = \frac{\lambda}{h \cdot c} \cdot T_{\text{det}}(\lambda) \cdot QE \cdot S_{\lambda}, \quad (15)$$

with  $\lambda$  the wavelength corresponding to the pixel,  $h$  Planck's constant,  $c$  the light velocity,  $QE$  the quantum efficiency of the detector, and  $T_{\text{det}}(\lambda)$  the sensitivity of the detector at the given wavelength.

All optical and mechanical elements that are entirely or partly "seen" by a pixel, contribute to the thermal background TB received by that pixel. The thermal background, i.e., the number of thermal photons generated by an element, is calculated based on the temperature-dependent thermal emission (Planck black-body equation), the emissivity and transmission of that element, and its etendue as viewed from the pixel. All elements situated in the optical path in front of the AOTFs are contributing very marginally to the thermal background, due to the filtering function of the AOTF. Only thermal background emitted in the selected passband of the AOTF can reach the detector. For the elements between the AOTF and

spectrometer slit the emitted thermal background is diffracted by the grating. Diffracted thermal background from all the grating orders will sum up on a pixel. For all elements after the spectrometer slit (slit included) the full thermal background (i.e., all wavelengths) will be detected by a pixel. The thermal background, expressed in  $e^-/s$ , is obtained by introducing the quantum efficiency of the detector.

The noise  $N$  of the channels is the sum of different noise contributions:

$$N = N_{\text{dark}} + N_{\text{ro}} + N_{\text{quant}} + N_{\text{shot}} + N_{\text{tb}}. \quad (16)$$

The dark current noise  $N_{\text{dark}}$  and pixel electronics readout noise  $N_{\text{ro}}$  are both fixed noises and given in the datasheet of the MARS MW detector ( $6000 e^-/s$  and  $1000 e^-/\text{pixel}$ , respectively). The quantization noise  $N_{\text{quant}}$  is the noise that originates from the fact that the signal is digitized over a limited number of bits  $n$  ( $n = 14$  for NOMAD) and is higher for higher signal  $S$  and thermal background  $TB$ . The shot noise  $N_{\text{shot}}$  is the noise resulting from the signal impacting the detector (square root of  $S$ ), the thermal background noise  $N_{\text{tb}}$  is

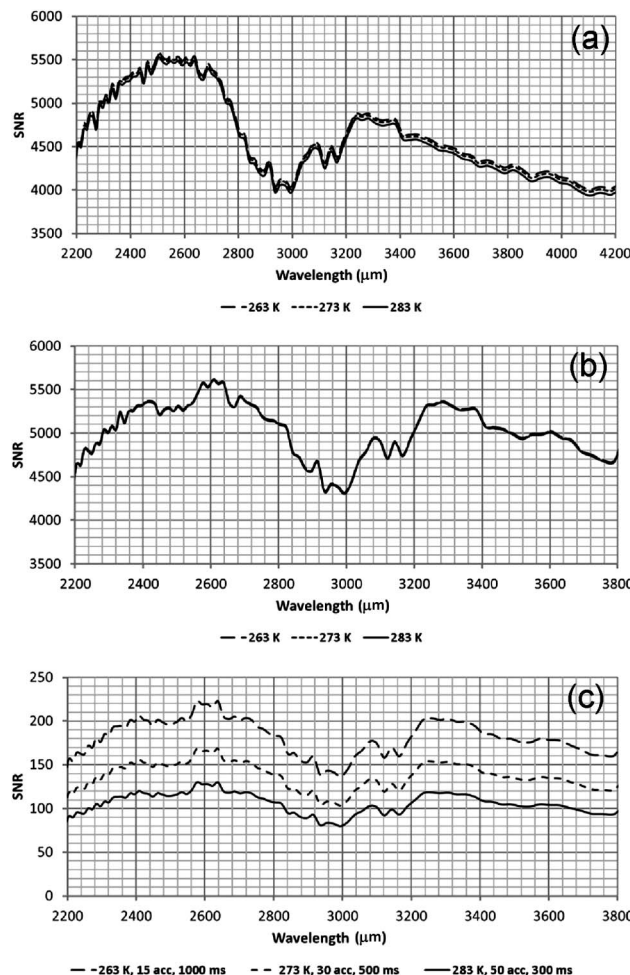


**Fig. 29.** (a) Single pixel SNR in SO (8 ms integration time). (b) Single pixel SNR in LNO (SO mode) (2.5 ms integration time). (c) SNR in LNO (nadir mode) (144 pixels binned, see legend of plot for integration time and number of accumulations).

the noise in the detector produced by the thermal background (square root of  $TB$ ). Equation (16) can be written as

$$N = \frac{S + TB}{\sqrt{12 \cdot 2^n}} + \sqrt{S} + \sqrt{TB} + Cte. \quad (17)$$

The SNR of a detector pixel in the NOMAD channels is obtained taking into account all of the above signal and noise sources. The SNR depends on the time the pixel is exposed to the signal and the noise sources. Therefore, an integration time has to be chosen that keeps the total charge below the saturation limit of the pixel, i.e., below its full well capacity ( $14.8 \cdot 10^{-6}$  or  $36 \cdot 10^{-6} e^-$  depending on the gain setting).

Figure 29 gives the SNR values for the SO and LNO channels, at the central wavelengths of the orders, for typical integration times and for three different realistic temperatures (263 K, 273 K, 283 K). For SO and LNO in SO mode the figure gives the single pixel SNR values (no binning, no accumulations). In the LNO channel working in nadir mode the pixels from one detector column have been binned over the slit height (144 pixels) and individual spectra have been accumulated over the duration of a measurement (15 s). Hence, for LNO in nadir mode the values in Fig. 29 are the single pixel SNR values multiplied by the square root of the binning factor and the square root of the number of accumulations. The SNR can vary quite significantly over the pixels in a row (or over the columns in the detector).

Full optical and radiometric models for the SO and LNO channels, including SNR calculations, are described in [16].

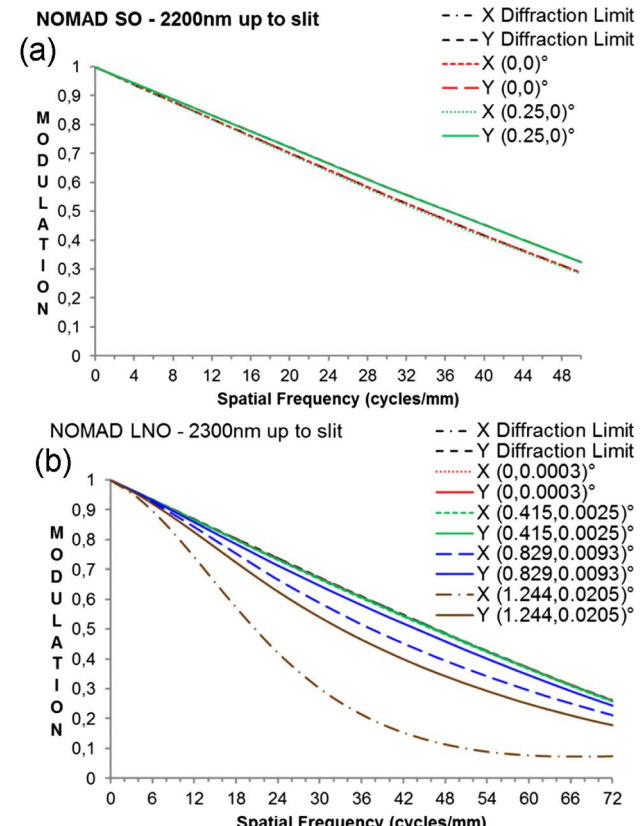


**Fig. 30.** MTF for optics in front of spectrometer slit. (a) SO, 2.2  $\mu\text{m}$  and (b) LNO, 2.3  $\mu\text{m}$ .

### 13. OPTICAL AND SPECTRAL PERFORMANCE

#### A. Image Quality of the Slit Image on the Sun

A section of the observed source (Sun, Mars) is imaged on the spectrometer slit by the optics in front of the slit. To assess the image quality of these optics it is investigated how, inversely, the slit is imaged on the source. During nadir measurements (LNO), where a measurement lasts typically 15 s and the space-craft moves with a relative ground velocity of 3 km/s, smearing will occur and a good image quality is not crucial. During SO measurements, however, a sharp image of the slit is needed (only the central 24 lines are used) with good image quality perpendicular to the slit (Y-direction). The modulation transfer function (MTF) of a system indicates how “faithfully” a subject (a line pattern expressed in cycles/mm) is transferred to its image by the system and, hence, is a measure for the image quality.

It is seen in Fig. 30 that for SO the MTF of the optics is close to being diffraction-limited (i.e., only limited by the wave

nature of the light itself and the finite diameter of the optical elements) for all wavelengths and for all positions in the slit. For LNO the optics are also close to diffraction-limited but show some deviation at lower wavelengths (e.g., 2.3  $\mu\text{m}$ ) for positions close to the edges of the slit in the Y-direction and away from the center in the X-direction (parallel to the slit).

By convoluting the optics’ point spread function (PSF) (i.e., the image the system makes of a point source) with a step function representing the geometrical size of the slit, the intensity profile of the image on the Sun is obtained. Figure 31 shows that this profile is 2' (SO) resp. 4' (LNO) wide (FWHM) corresponding nicely to the respective widths of the NOMAD slits.

#### B. Image Quality on the Detector

The optics between the slit and the detector form an image of the slit on the detector that is spectrally dispersed. To define the image quality in the Y-direction (i.e., the direction perpendicular to the slit) only the optics between the slit and the detector have to be taken into account, since in that direction the optics in front of the slit serve only to illuminate the slit (the object is a point source at the slit). In the X-direction (i.e., the direction along the slit) the image quality depends on the complete optics from entrance till detector (the object is a point source at infinity in front of the instrument). The MTF at the focal plane position of the SO and

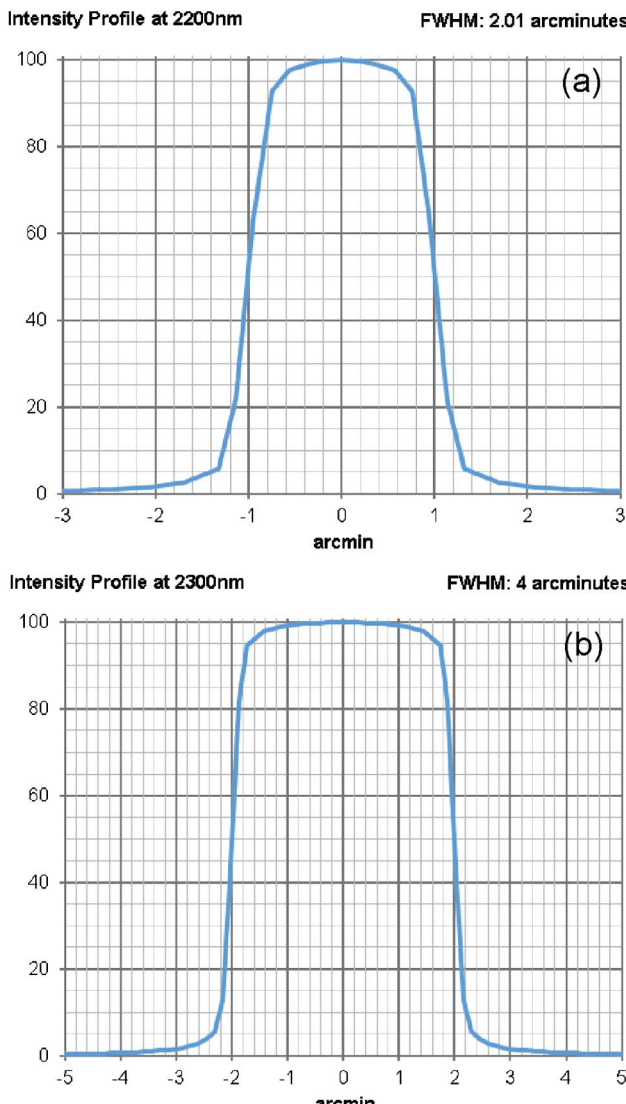


**Fig. 31.** Intensity profile of slit image on the Sun [(a): SO and (b): LNO] at 2.2  $\mu\text{m}$  resp. 2.3  $\mu\text{m}$ .

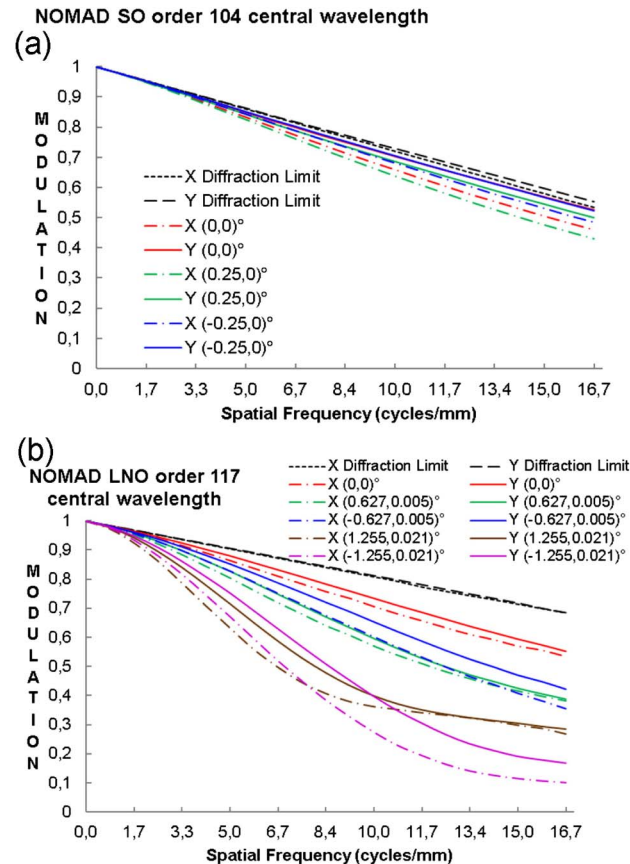


**Fig. 32.** MTF for optics between spectrometer slit and detector. (a) SO, order 104, central wavelength 4.26  $\mu\text{m}$ . (b) LNO, order 117, central wavelength 3.77  $\mu\text{m}$ .

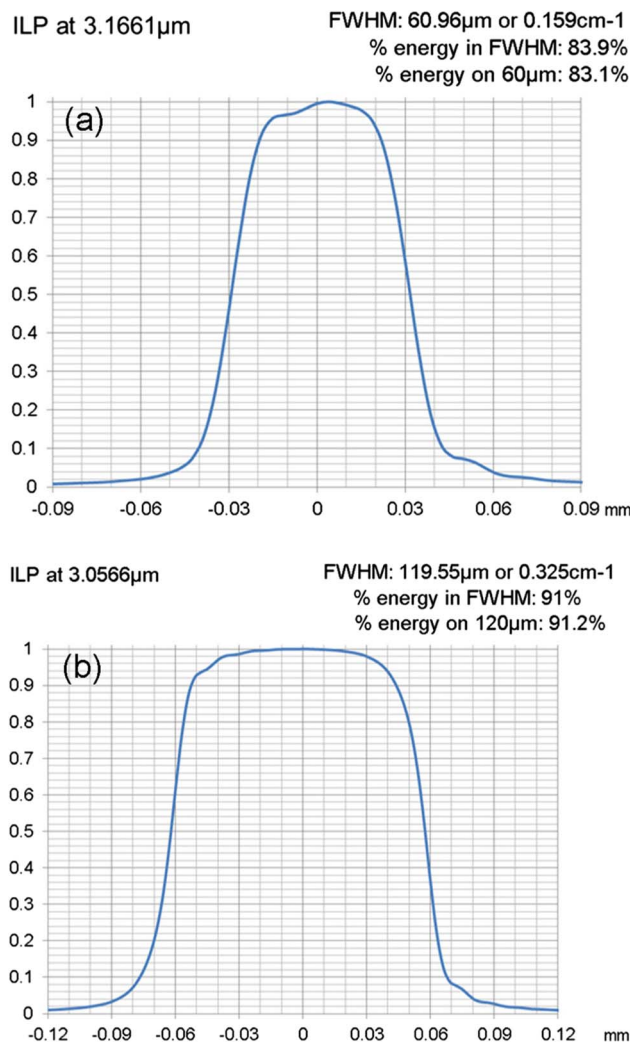


**Fig. 33.** ILP for the central wavelength in order 140 [(a) SO] and order 145 [(b) LNO].

LNO detector is calculated for both the spectral Y-direction and the spatial X-direction and plotted in Fig. 32 for the central wavelength  $\lambda_c$  (corresponding to the center of the detector) in

only one order (104 for SO, 117 for LNO), for different positions on the slit and up to the Nyquist frequency of the detector (16.7 cycles/mm). Similar plots can be obtained for all other orders and for wavelengths imaged at the edge of the free spectral range of an order or at the edge of the detector. In SO the MTF at the Nyquist frequency and at the central wavelength  $\lambda_c$  is always  $\geq 0.4$  in both the X- and the Y-direction. In LNO it is lower especially toward the edges of the slit (0.17 for the Y-direction) and the edges of the illuminated zone (0.1 for the X-direction). On top of that, at the “spectral” edges (and especially at the low wavelengths in the orders) the image quality degrades further (0.18 in SO and 0 in LNO).

### C. Smile and Frown

Smile occurs in a spectrometer when its slit is not imaged as a straight line on the detector and, as a consequence, pixels in one detector column see slightly different wavelengths. A point source at the center of the spectrometer slit is imaged, for a specific wavelength, through the PSF of the system, as a spot on the detector. The center of this spot is used as zero reference for the smile. Other points on the slit, away from the center along the X-direction, are imaged on the detector but can deviate in the Y-direction from the zero reference. The Y-difference between the center of a spot and the center of the reference spot, all for the same wavelength, is a measure of the smile. It can be expressed in pixels or in  $\text{cm}^{-1}$  after conversion by means of the spectral sampling interval, which varies over orders and over pixels inside an order. In SO the smile at a given wavelength is always  $\leq 0.1$  pixels. In LNO the smile over the central 24' (SOs) is  $\leq 0.15$  pixels while over the full slit height of 150' (nadir) it is  $\leq 0.8$  pixels. In LNO a curved slit is used to compensate for the smile (see above).

Frown occurs when a specific point in the optical field is not imaged at the same height (i.e., in the same row) on the detector for all wavelengths. A point source in the field of the instrument is imaged, for the central wavelength  $\lambda_c$  of a specific order, as a spot on the detector. The center of this spot is used as the zero reference for the frown. For the same point in the field, but for other wavelengths in that same order, spots are formed at the detector that can deviate in the X-direction from the zero reference. The X-difference between the center of a spot and

**Table 12. Dispersion, Theoretical ILP, Predicted ILP, Energy Fraction for Central Wavelengths  $\lambda_c$  in SO**

Order	$\lambda_c$ [μm]	$\partial\lambda/\partial D$ [cm⁻¹/mm]	Theoretical ILP (FWHM) [cm⁻¹]	Predicted ILP (FWHM) [cm⁻¹]–[μm]	Energy fraction [%]⁴–[%]⁵
100	4.4302	1.88	0.113	0.116–63.21	78.79–77.12
110	4.0275	2.07	0.124	0.128–63.12	79.40–77.82
120	3.6919	2.25	0.135	0.139–63.02	80.01–78.52
130	3.4079	2.44	0.146	0.150–62.92	80.62–79.22
140	3.1661	2.63	0.158	0.161–62.82	81.22–79.92
150	2.9535	2.82	0.169	0.173–62.72	81.83–80.62
160	2.7689	3.01	0.181	0.184–62.63	82.44–81.31
170	2.6060	3.19	0.191	0.195–62.53	83.05–82.01
180	2.4612	3.38	0.203	0.206–62.43	83.66–82.71
190	2.3317	3.57	0.214	0.218–62.33	84.27–83.41
200	2.2151	3.76	0.226	0.229–62.24	84.88–84.11

<sup>a</sup>FWHM.

<sup>b</sup>2 pixels.

**Table 13.** Dispersion, Theoretical ILP, Predicted ILP, Energy Fraction for Central Wavelengths  $\lambda_c$  in LNO

Order	$\lambda_c$ [μm]	$\partial\lambda/\partial D$ [cm <sup>-1</sup> /mm]	Theoretical ILP (FWHM) [cm <sup>-1</sup> ]	Predicted ILP (FWHM)[cm <sup>-1</sup> ]–[μm]	Energy fraction [%] <sup>a</sup> –[%] <sup>b</sup>
120	3.6914	2.26	0.271	0.247–123,56	81,59–80.79
130	3.4076	2.44	0.293	0.296–123,42	81,77–81.02
140	3.1641	2.63	0.316	0.319–123,28	81,95–81.26
150	2.9531	2.82	0.338	0.341–123,15	82,13–81.49
160	2.7686	3.01	0.361	0.364–123,01	82,31–81.73
170	2.6057	3.20	0.384	0.386–122,87	82,50–81.97
180	2.4609	3.39	0.407	0.409–122,73	82,68–82.20
190	2.3314	3.57	0.428	0.431–122,60	82,86–82.44
200	2.2148	3.76	0.451	0.454–122,46	83,04–82.67

<sup>a</sup>FWHM.<sup>b</sup>4 pixels.

the center of the reference spot, all for the same field point, is a measure for the frown. In SO the frown for a given field point in a given order is always  $\leq 0.5$  pixels. In LNO the frown for field points situated in the central 24' (SOs) is  $\leq 0.65$  pixels, while for field points situated in the full 150' (nadir) it is  $\leq 1.8$  pixels.

#### D. Instrument Line Profile

The ILP of a system is the energy distribution on the detector when the spectrometer slit is completely illuminated with monochromatic light. The theoretical ILP that can be expected

based on the grating parameters, is obtained by multiplying the dispersion (Tables 7 and 8) with the width of the spectrometer slit (60 μm in SO, 120 μm in LNO). The results are given in Tables 12 and 13. The predicted ILP for the full NOMAD channels is obtained in three steps: (1) calculate the PSF of a point source in a number of positions along the height of the slit (or the useful part), (2) make the convolution of these PSFs with a square step function representing the geometrical size of the slit, (3) sum the Y-components of the convolution results. For LNO in nadir mode, where the used part of the slit is quite high, an additional step is needed, correcting for the smile of the system. Figure 33 gives an example of an instrument line

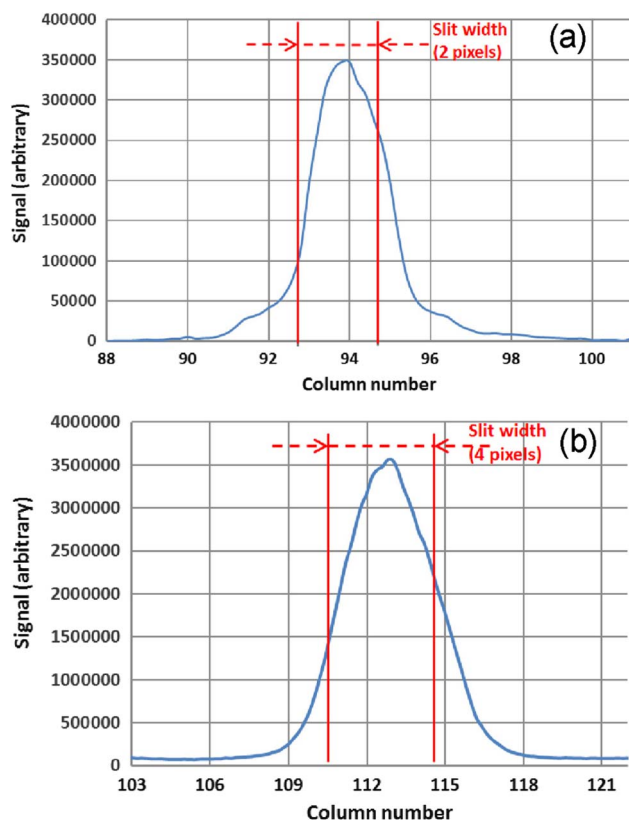


**Fig. 34.** ILP for detector row 132 [(a) SO] and averaged over 100 rows [(b) LNO] with slit illuminated by monochromatic laser light beam at 3.39 μm

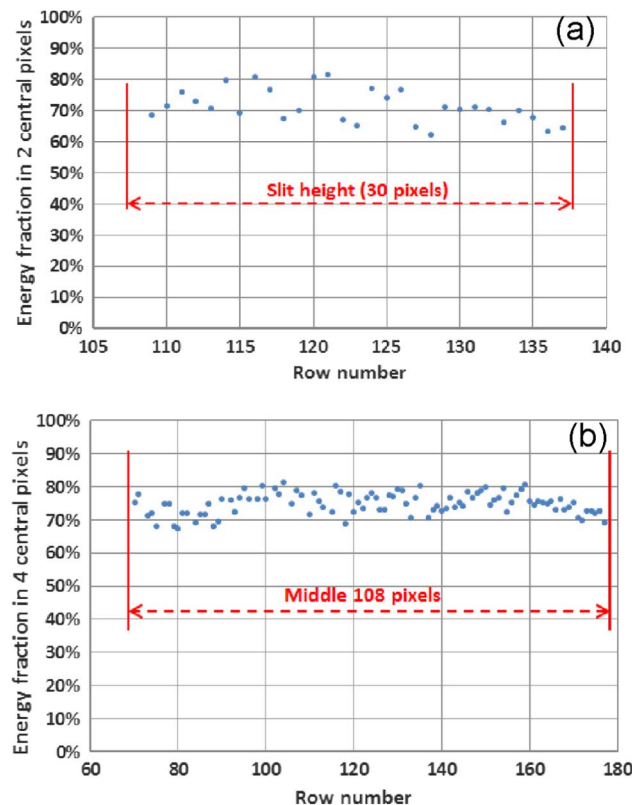


**Fig. 35.** Energy fraction in the two central pixels [(a) SO] and four central pixels [(b) LNO] over the slit height with monochromatic laser light beam at 3.39 μm.

profile for SO and LNO for the central wavelength  $\lambda_c$  in order 140 for SO and order 145 for LNO.

Tables 12 and 13 give a broader overview of the ILP values (FWHM) for the central wavelengths in the orders in SO resp. LNO, as well as the fraction of the total energy within FWHM and within two pixels (SO) or four pixels (LNO), taking into account the manufacturing tolerances. For SO the ILP (FWHM) varies between  $0.116 \text{ cm}^{-1}$  or  $63.21 \mu\text{m}$  (order 100) and  $0.226 \text{ cm}^{-1}$  or  $62.3 \mu\text{m}$  (order 200) with energy fractions in two pixels between 77% and 84%. For LNO the ILP (FWHM) varies between  $0.247 \text{ cm}^{-1}$  or  $123.56 \mu\text{m}$  (order 120) and  $0.454 \text{ cm}^{-1}$  or  $122.46 \mu\text{m}$  (order 200) with energy fractions in four pixels between 81% and 83%. The ILP (FWHM) for the wavelengths at the edge of the detector is slightly different from those in the center and the corresponding energy fraction is decreased at the edges by  $\leq 5\%$ .

### E. Verification with Laser

The predicted instrument line profile was checked in the lab with a diffused collimated laser light beam (at  $3.39 \mu\text{m}$ ) filling the spectrometer slit entirely for SO. For LNO a patchwork filling of the slit was performed over more than 100 rows. Figure 34 shows the ILP in detector row 132 for SO and the averaged ILP for LNO over all illuminated rows. For SO the ILP in row 132 is  $63.92 \mu\text{m}$  (2.13 pixels), with an energy fraction of 70.5% in the two central pixels, to be compared with the predicted values of  $62.9 \mu\text{m}$  and 79.4%. For LNO the averaged ILP is  $124.6 \mu\text{m}$  (4.15 pixels), with an energy fraction of 75.7% on the four central pixels, to be compared to a predicted average values of  $123.0 \mu\text{m}$  and 81.7%.

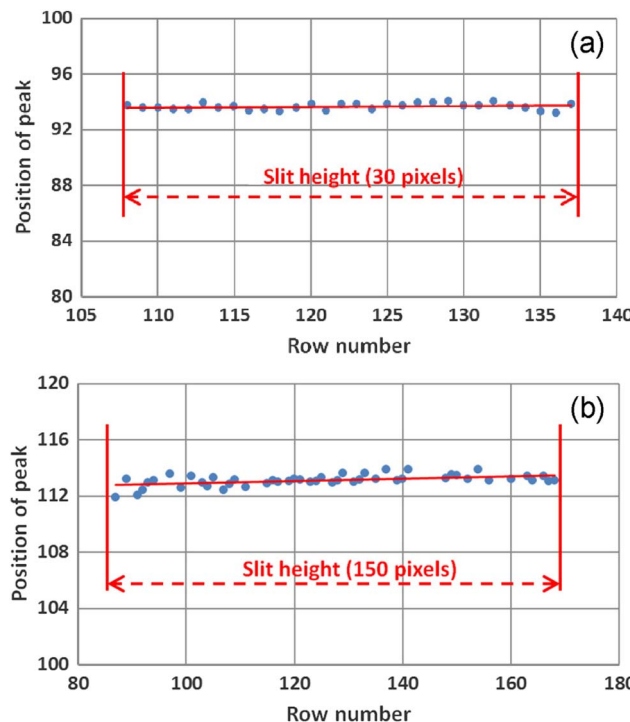


**Fig. 36.** Position of peak as a function of row number (measure for tilt and smile of the optical system). Measured with monochromatic laser light beam at  $3.39 \mu\text{m}$  [(a) SO and (b) LNO].

Because the source contains only light at one wavelength, a single image of the slit should appear on the detector, rather than a horizontal band. Figure 35 gives the energy fraction in the central two pixels for all 30 rows (for SO) and in the central four pixels for the middle 108 rows (for LNO) that are illuminated by the respective slits, proving that the slit is imaged on the detector as expected.

Figure 36 gives for SO and LNO the position of the peak (column number scale) for each detector row. From these plots it can be seen that in both channels no smile is observed. One can, however, see a small tilt of the slit image with respect to the detector columns. In SO this tilt is 0.153 pixels over the total slit height of 30 pixels; in LNO it is 0.71 pixels over 80 central pixels (measured) and 1.32 pixels over the total slit height of 150 pixels (extrapolated).

### F. Verification with Broad Light Source

Both the SO and LNO channel were tested in a clean room environment with a broad infrared light source. In Fig. 37 typical absorption spectra of the air in the lab are shown for one specific order (order 160 for SO at AOTF frequency 21.68 MHz, order 168 for LNO at AOTF frequency 24.31 MHz). The plots show 24 spectra, corresponding to individual detector lines in SO and to bins of six detector lines in LNO. At the time of this measurement the instrument

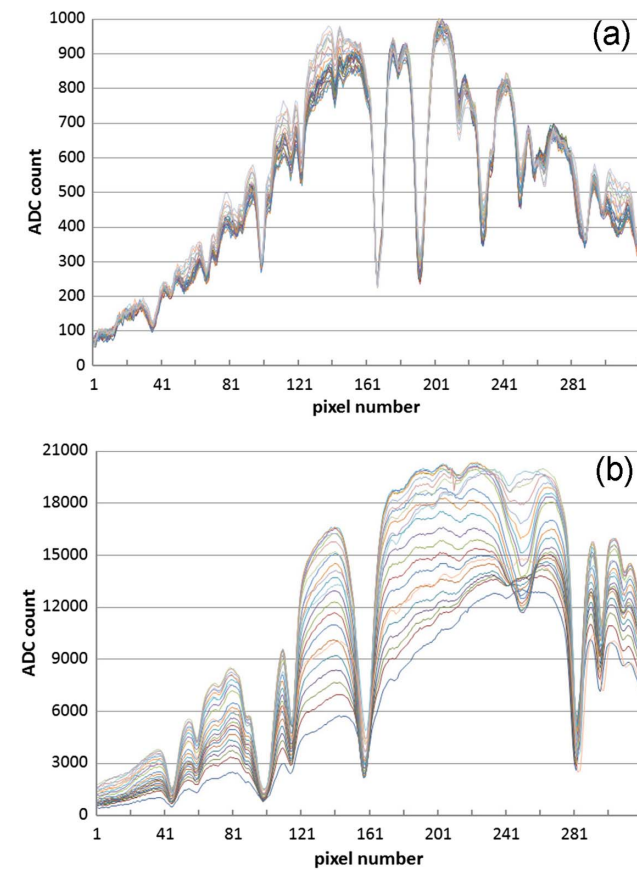


**Fig. 37.** Absorption spectra with SO [(a), order 160] and LNO [(b), order 168] of ambient air, registered with a broad infrared light source.

was not yet calibrated, hence the figures are just qualitative indications of the good functioning of the infrared channels. Extensive reporting on instrumental calibration is the subject of a separate paper [14].

## 14. CONCLUSIONS

In the conclusion of the paper that described the SOIR instrument on Venus Express [1] the following statement was made. "It is obvious that the field of applications for the spectrometer described is not limited to the Venus Express mission only. It could be extremely useful to study the presence of methane in the Martian atmosphere by solar occultation (SO), and this spectrometer could perform such a task with a 10-times-higher spectral resolution than is possible with present instruments in orbit around Mars." With the trace gas orbiter of ExoMars, to be launched in January 2016, ESA offered a wonderful occasion to achieve this goal. This is why the first objective during the conception of NOMAD was to fly to Mars a one-to-one copy of the extremely successful SOIR instrument. The SO channel of NOMAD, which is described in this paper, will offer good spectral resolution, high vertical sampling, and excellent sensitivity during SOs.

While SOIR was limited to SO measurements only, mass and volume settings for NOMAD allowed for a significant upgrade of the instrument. It was the goal to add, on top of the SO channel, a second SOIR-like instrument, with more or less the same spectral characteristics but increased sensitivity, capable of performing measurements with much weaker light sources than the Sun (nadir, limb). A key element to come to this unprecedented performance was an extreme cooling of the spectrometer section to  $-100^{\circ}\text{C}$ . The LNO channel, described in this paper, does not have this capability. The cryoradiator and spectrometer cryosection, the development of which was already far set, was descoped due to programmatic constraints and resource limitations. A suite of other measures has been taken to increase the SNR of the LNO channel so that nadir measurements with NOMAD will at least partially comply with the initial requirements.

All in all the NOMAD instrument, which besides the two infrared channels also contains a channel operating in the ultraviolet and visible wavelength range (not described in this paper), is bound to deliver Martian atmospheric science beyond the present knowledge thanks to a unique combination of spectrometric performances.

**Funding.** Belgian Science Policy Office (BELSPO) (4000103401, 4000103402); ESA Prodex Office; Ministerio de Ciencia e Innovación (MICINN) (AYA2012-39691-C02-01, AYA2012-39691-C02-02); Science and Technology Facilities Council (STFC) (ST/I003061/1); UK Space Agency (UKSA).

**Acknowledgment.** The NOMAD instrument has been developed under the responsibility of a Belgian principal investigator team (BIRA-IASB, Brussels), assisted by Co-PI teams from Spain (IAA-CSIC, Granada) and the United Kingdom (OU, Milton-Keynes). Associated teams contributing to the design and development of NOMAD were CSL (Liège, Belgium),

IFSI (Rome, Italy), and IDR-UPM (Madrid, Spain). We thank all engineering and supporting personnel in these teams for the hard and solid work. Several industrial partners were associated with the above-mentioned teams. The industrial efforts were coordinated by a Belgian prime contractor (OIP, Oudenaarde). The following industrial associates, partners, or subcontractors have contributed to NOMAD: AMOS (Liège, Belgium), Deforce (Izegem, Belgium), ERZIA (Santander, Spain), ESTEC (Noordwijk-aan-Zee, Netherlands), Glenair (Mansfield, United Kingdom), Gooch and Housego (Ilminster, United Kingdom), HPS (München, Germany), Lambda-X (Nivelles, Belgium), MAP (Pamiers, France), Protection des Métaux (Noisy le Sec, France), Sener (Barcelona, Spain), Sofradir (Grenoble, France), Thales Alenia Space Belgium (Charleroi, Belgium), Thales Alenia Space France (Conflans Sainte Honorine, France), Vaskon (Oudenaarde, Belgium). An important part of the work described in this paper, and especially the outstanding optical design work, has been conducted by Wouter Moelans and Ludovic Aballea at OIP. Our gratitude also goes to Dennis Nevejans and Emiel van Ransbeeck, who, although retired, gave invaluable advice and support to the team at BIRA-IASB. Finally, our deepest respect to Stefan Lesschaeve, system engineer at OIP, who sailed NOMAD safely through heavy weather. We are very grateful to ESA for giving the scientific community the chance to go to Mars (once more) and for persisting when the project was in danger. Our warmest thanks to the ExoMars TGO project team at ESA and especially to André Debus, who followed the development of NOMAD from start to finish.

## REFERENCES

1. D. Nevejans, E. Neefs, E. Van Ransbeeck, S. Berkenbosch, R. Clairquin, L. De Vos, W. Moelans, S. Glorieux, A. Baeke, O. Koralev, I. Vinogradov, Y. Kalinnikov, B. Bach, J.-P. Dubois, and E. Villard, "Compact high-resolution spaceborne echelle grating spectrometer with acousto-optical tunable filter based order sorting for the infrared domain from 2.2 to 4.3  $\mu\text{m}$ ," *Appl. Opt.* **45**, 5191–5206 (2006).
2. A. Mahieux, A. C. Vandaele, S. Robert, V. Wilquet, R. Drummond, F. Montmessin, and J. L. Bertaux, "Densities and temperatures in the Venus mesosphere and lower thermosphere retrieved from SOIR on board Venus Express: carbon dioxide measurements at the Venus terminator," *J. Geophys. Res.* **117**, E07001 (2012).
3. V. Wilquet, R. Drummond, A. Mahieux, S. Robert, A. C. Vandaele, and J. L. Bertaux, "Optical extinction due to aerosols in the upper haze of Venus: four years of SOIR/VEX observations from 2006 to 2010," *Icarus* **217**, 875–881 (2012).
4. A. C. Vandaele, A. Mahieux, S. Robert, R. Drummond, V. Wilquet, and J. L. Bertaux, "Carbon monoxide short term variability observed on Venus with SOIR/VEX," *Planet. Space Sci.* (to be published).
5. M. Patel, "The NOMAD spectrometer on the ExoMars trace gas orbiter mission: part 2—design and testing of the ultraviolet and visible channel," (in preparation).
6. "EXOMARS. Planetary exploration mission. Mars planet in-situ," [smsc.cnes.fr/EXOMARS/OLD/GP\\_lander.htm](http://smsc.cnes.fr/EXOMARS/OLD/GP_lander.htm).
7. A. C. Vandaele, E. Neefs, R. Drummond, I. R. Thomas, F. Daerden, J.-J. Lopez-Moreno, J. Rodriguez, M. R. Patel, G. Bellucci, M. Allen, F. Altieri, D. Bolsée, T. Clancy, S. Delanoye, C. Depiesse, E. Cloutis, A. Fedorova, V. Formisano, B. Funke, D. Fussen, A. Geminale, J.-C. Gérard, M. Giuranna, N. Ignatiev, J. Kaminski, O. Karatekin, F. Lefèvre, M. López-Puertas, M. López-Valverde, A. Mahieux, J. McConnell, M. Mumma, L. Neary, E. Renotte, B. Ristic, S. Robert, M. Smith, S. Trokhimovsky, J. Vander, Auwera, G. Villanueva, J.

- Whiteway, V. Wilquet, and M. Wolff, The NOMAD Team, "NOMAD, a spectrometer suite for the ExoMars mission," in preparation.
- 8. C. Palmer, *Diffraction Grating Handbook*, 6th ed. (Newport, 2005).
  - 9. M. C. Hutley, "Diffraction gratings," in *Techniques of Physics* (Academic, 1982), Vol. 6, pp. 76.
  - 10. B. W. Bach, Jr., K. G. Bach, M. Schulze, and B. Bach, Jr., "Modern echelons and echelles for infrared spectroscopy," Proc. SPIE **5901**, 184–190 (2005).
  - 11. M. S. Gottlieb, "Acousto-optic tunable filters," in *Design and Fabrication of Acousto-Optic Devices*, A. P. Gotzoulis, D. R. Pape, and S. V. Kulakov, eds. (Marcel Dekker, 1994), pp. 197–283.
  - 12. I. C. Chang, "Non-collinear acousto-optic filter with large angular aperture," Appl. Phys. Lett. **25**, 370–372 (1974).
  - 13. "MARS MW 320 × 256—30 μm pitch—MCT. The reference for MWIR 320 × 256 detectors," [www.sofradir.com](http://www.sofradir.com).
  - 14. I. Thomas and C. Depiesse, "NOMAD, calibration of three spectrometer channels," in preparation.
  - 15. "ASTM E490-00a(2014) standard solar constant and zero air mass solar spectral irradiance tables," [www.astm.org](http://www.astm.org).
  - 16. I. R. Thomas, A. C. Vandaele, S. Robert, E. Neefs, R. Drummond, F. Daerden, S. Delanoye, C. Depiesse, B. Ristic, A. Mahieux, L. Neary, Y. Willame, V. Wilquet, L. Aballea, W. Moelans, L. De Vos, S. Lesschaeve, N. Van Vooren, J.-J. Lopez-Moreno, M. Patel, and G. Bellucci, The NOMAD Team, "Optical and radiometric models of the NOMAD instrument. Part II: the infrared channels, SO and LNO," in preparation.